Understanding Proton Dynamics in Cement Pastes

A Quasi-Elastic Neutron Scattering Study

Johan Jacobsen

Copenhagen 2013
NBI-M.Sc.-2013

University of Copenhagen
Faculty of Science
Niels Bohr Institute
NBI-M.Sc.-2013

Preface

This thesis was prepared at the Niels Bohr Institute at the University of Copenhagen in fulfillment of the requirements for acquiring a MSc. degree in Physics, and financed by the European Spallation Source, ESS AB. Associate professor Heloisa Nunes Bordallo from the Niels Bohr Institute was the main supervisor, assistant professor Ana Raquel Benetti from the Panum Institute at the University of Copenhagen and Dr. Markus Strobl from the ESS AB were co-supervisors.

Copenhagen, 11-July-2013

Johan Jacobsen

Summary

This work is divided in 6 chapters. Chapter 1 gives a broad overview of the hydration process in two different cementitious materials; construction cement and dental cement. This is followed by a summary of the use of neutron scattering, and particularly quasi-elastic neutron scattering, to study proton motion.

Chapter 2 deals with the necessary theoretical background of quasi-elastic neutron scattering (QENS).

Chapter 3 explains the elastic fixed window (EFW) and QENS methods in more detail. Also it describes the backscattering technique and accounts for the information that can be retrieved from the experiment. Furthermore the steps needed to treat the data prior to analysis are explained and the methods used in analyzing the data are described.

Chapter 4 investigates two types of construction cement, one is ordinary Portland cement (OPC), the other is an OPC that has been supplemented with ashes from sugar cane bagasse provided by the co-generation industry. The addition of pozzolanic materials, such as ash, to the cement has a positive effect on the ability to limit fluid transmission by binding water in calcium silicate hydrates (C-S-H)[1]. By comparing the motion of the *confined water* in the two samples, it can be determined how the inclusion of pozzolanic ashes changes the proton motion and thus how proton mobility and cement strength are related. The samples studied were prepared by Michelle Santos Rodrigues at the School of Agricultural Engineering / FEAGRI, UNICAMP, São Paulo, Brazil as part of her Ph.D. project. The experiment was conducted in early December 2011 at the high resolution backscattering spectrometer IRIS at the ISIS facility, Rutherford Appleton Laboratory in the UK.

Chapter 5 discusses the hydration process of two dental restorative glass ionomer cements (GIC), Aqua Ionofil Plus and Ionofil Molar AC. The former is a GIC where polyacid is incorporated in the powder component and the liquid component is water, while the latter has the polyacid as part

of the liquid component. Both have been provided by the dental materials company Voco [2]. The hydration processes are seen by neutrons in two different time windows, one covering motions in the picosecond (ps) range and the other in the nanosecond (ns) range. It is known that Aqua Ionofil Plus has a longer setting time than Ionofil Molar AC, which allows for longer application time during the restorative work. The durability and structural strength of Aqua Ionofil Plus is, however, less than that of Ionofil Molar AC. This investigation involved studying the evolution of the hydrogen mobility in the two dental cement types, during the first 24 hours of the setting process, and again after $4-5$ days of maturation. Comparing this evolution in the two cements allows the determination of how the hydrogen mobility is linked to the setting time and the final strength of the two cements. These experiments were conducted in March 2012 at the high resolution backscattering spectrometer IRIS at the ISIS facility, Rutherford Appleton Laboratory in the UK and in November 2012 at the high resolution backscattering spectrometer IN10 at the Institute Laue-Langevin in Grenoble, France.

Chapter 6 summarizes the results of the construction cement and dental cement experiments.

Acknowledgements

First and foremost, I would like to thank Heloisa Nunes-Bordallo for the opportunity to participate in her amazing projects, visit impressive neutron scattering facilities and conduct exciting and useful research.
Michelle Santos Rodrigues for without her there would be no green cement to study.
Ana Raquel Benetti for her invaluable help with understanding dental materials, preparing samples and helping make my thesis comprehensible for non-physicists.
Voco for supplying material for our dental cement samples.
Markus Strobl for his support and rational calming presence in times of stress.
Luke Herbert for his incredible LaTex expertise.
Niels Christian Momsen for his assistance with the IN10 data analysis and his company during otherwise long hours in the ILL guide hall.
Mark Telling and Tilo Seydel whose help as instrument scientists has proven invaluable, both during the experiment and afterwards when analyzing the data.
Finally I would like to thank my wife Sascha for bearing with me in my more aggravating and stressful periods.

Table of Contents

Chapter 1

Cement, Hydration and Neutrons

A cement is in essence a binder. A material that sets, hardens and binds things together. Cement can be many different materials used in a wide variety of ways. In this master's thesis I will deal with two very different cements - construction cement and dental cement. While each has its own distinct problems that need to be understood, the method used to understand them is the same, namely neutron scattering. In this chapter I will explain the problems concerning each of the two cements, briefly elucidate the concept of neutron scattering and explain the strengths of this technique when applied to the study of cement.

1.1 Green Concrete

The increasing demand for energy sources such as coal, natural gas and oil has lead to an increased focus on alternative energy sources. One such source, which has been utilized for years, stems from the sugarcane agro-industry. The extraction of sugar from sugarcane leaves behind a waste product called sugar cane bagasse as well as the removed sugarcane leaves and cane tops. While the extracted sugar is effectively used as a source for bio-ethanol, it is in competition with food production [3]. The bagasse, leaves and cane tops are fibrous materials with much biotechnological potential, for example as a less effective source of bio-ethanol or for paper production [4]. However approximately 50% is stockpiled, while the rest is used as biofuel [3]. The bagasse used for biofuel is dried and burned to provide heat and electricity in a process known as co-generation [5]. In this manner, all the heat and energy needs of the sugar mills are provided from bagasse waste, while excess electricity is sold on the market. The downside is that a new waste material is created, called bagasse ash.

This ash is usually deposited in landfills where it awaits re-utilization as raw material in other industrial sectors, such as the concrete industry. In recent years, the research related to agricultural wastes which aims to evaluate their potential for recycling and eliminate the landfills, has increased dramatically [6]. The bagasse ashes are recognized as having pozzolanic properties [7]. This means that while the ashes have little or no cementitious properties, they will chemically, in the presence of water, react with calcium hydroxide to form materials with cementitious properties. They can then be used as alternative supplementary cementitious materials for concrete production. Since the cement industry produces about 5% of global man-made CO_2 emissions [8], the use of supplementary cementitious materials in concrete production will have a positive effect on the reduction of global CO_2 emission.

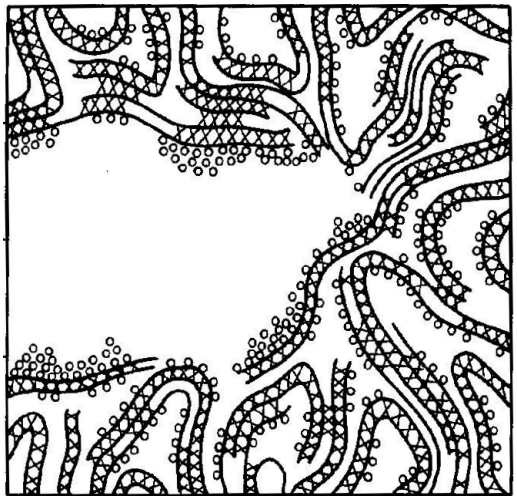

Figure 1.1: *A large capillary pore embedded in the C-S-H structure and surrounded by smaller gel pores. As the cement matures, water will move from the capillary pores to the gel pores. Besides this effect, some of the water binds to the cement matrix as H_2O and OH groups. Figure is adapted from [9].*

Concrete is a composite material consisting of aggregate, cement and water. The cement serves as a binder for the aggregate, and when water is mixed with the cement it becomes cement paste, which can be poured and shaped. The cement paste then slowly solidifies through a process known as hydration [10], forming calcium silicate hydrate (C-S-H):

$$Ca_3SiO_5 + H_2O \rightarrow (CaO) \cdot (SiO)_2 \cdot (H_2O) + Ca(OH)_2 \qquad (1.1)$$

During this hydration process, the water becomes trapped within the developing pore structure and gradually moves from the large capillary pores into the smaller gel pores. Figure 1.1 illustrates the cement pore structure. Capillary pores are pores with an average radius greater than 50 Å, while gel pores are pores with an average radius less than 50 Å [11]. Besides this effect, some of the water binds to the cement matrix as H_2O and OH groups [10].

The strength of a cement is dependent on its ability to hinder water movement through the pore structure, as this movement results in erosion and formation of cracks, thus weakening the structure [12]. Therefore, understanding the mobility of the water located in the capillary and gel pores, as well as the *bound water*, is crucial to understanding the concrete's strength.

1.2 Dental Cement

The extent of caries continues to be a major global health problem. The last decade has shown a clear increase in the global prevalence of dental caries [13][14], despite improved preventive therapies and an increased understanding of the disease.

The earliest sign of caries infection is the appearance of a chalky white spot on the surface of a tooth. If left untreated it will progress into the formation of cavities and ultimately cause tooth loss. Although there has been extensive development in materials [15] and available technology, treatment options have not followed in the same pace. The extensive development has however, made diverse treatment options available for the sequelae of caries. The lost dental structure as a result of untreated caries can be replaced by dental fillings, crowns, bridges, or implants, either separately or as a combination. There has also been a significant focus on preventive therapies, as practice has shifted towards treating the disease rather than its consequences. This has resulted in many advances such as the use of fluorides and non-restorative treatments [16].

The idea of filling decayed teeth with metal alloys, and the subsequent introduction of dental amalgams containing mercury, dates back to the beginning of the 19th century. Their use and the consequences of the high mercury content have been debated for 150 years [17]. Around the year 1900, a high

content silver alloy was introduced and this formed the basis for the conventional dental amalgam still used today [18]. The adverse effects on the environment and possibly the human health as a result of mercury exposure, combined with the availability of alternative materials, has lead to a recent ban of dental amalgam in some countries and increased control of its use in others.

In the perspective of preventive dentistry, glass ionomer cements (GIC) are an interesting alternative to dental amalgam. They contain and release fluoride, which helps to prevent caries lesions, have a thermal expansion coefficient similar to the tooth structure and bond chemically to dentin and enamel during the setting process [19].
Despite the advantages of GIC over other restorative materials, their weaker mechanical strength has been a hindrance to their application [20]. For this reason, this study deals with GIC to understand how its mechanical strength can be improved. An important step is to understand the hydration process during the setting and maturation periods. Glass ionomer cements are chemically set via an acid-base reaction. Upon mixing the glass and polyacid components, the glass is dissolved into a gel which hardens within minutes and continues to evolve for days. Water plays a crucial part in the formation and maturation of the dental cement, initially as the reaction medium and later, through the hydration of calcium and aluminum polysalts, as the link which gives strength to the gel structure [19]. The speed with which the hydration takes place, as well as the total fraction of bound hydrogen, are directly related to the strength of the GIC [19].

1.3 Water Mobility Seen by Neutrons

Neutron scattering is ideally suited to study water in confinement. The two main reasons for this are the ability of neutrons to penetrate most materials easily [21] and the high incoherent scattering cross section of hydrogen compared to other elements [22]. Therefore, the hydrogen in water and hence also water itself is highly visible to neutrons. Figure 1.2 shows an example of the application of these two properties [23]. Here water transport through cement was studied using neutron radiography. The neutrons penetrate the cement and the water front is clearly seen moving through the cement over time.

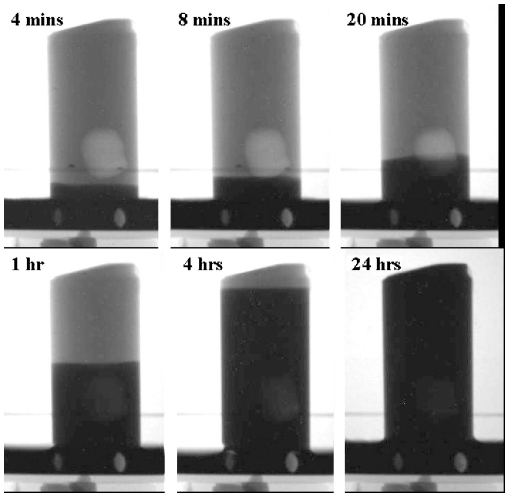

Figure 1.2: *The ability of neutrons to easily penetrate most samples allows for the bulk of a cement pillar to be examined. The samples shown here are* 25 *mm diameter and* 50 *mm high. The high incoherent scattering cross section of hydrogen causes the water (dark area) to be highly visible within the cement, allowing for its transport through the cement to be studied [23].*

Quasi-elastic neutron scattering (QENS) is a special type of neutron scattering. It provides information on the type and geometry of the studied motion. In a QENS experiment, the measured intensity is proportional to the scattering function, $S(Q, \omega)$, which can be decomposed into three parts: an elastic (E) part, a quasi-elastic (QE) part, and an inelastic (IN) part [24]. The width of the E signal is determined by the instrument resolution that also determines the time scale in which the motions can be resolved.

Figure 1.3 shows that the E part of $S(Q, \omega)$ will contain the signal from structurally bound hydrogen or hydrogen moving too slowly to be seen in the investigated time scale. The wings, i.e. the broad part of the signal, contain the contributions from fast-moving hydrogen. For example *bulk-like* water that diffuses freely through the sample. In between these two lies the QE part. This contains information on the mobile hydrogen whose motion is somewhat restricted, which prevents it from moving freely through the sample, e.g. water confined in the gel pores of cement. The QE part of the signal can be modeled by one or more Lorentzian functions. The width of these functions can be related to the time-scale of the attributed mo-

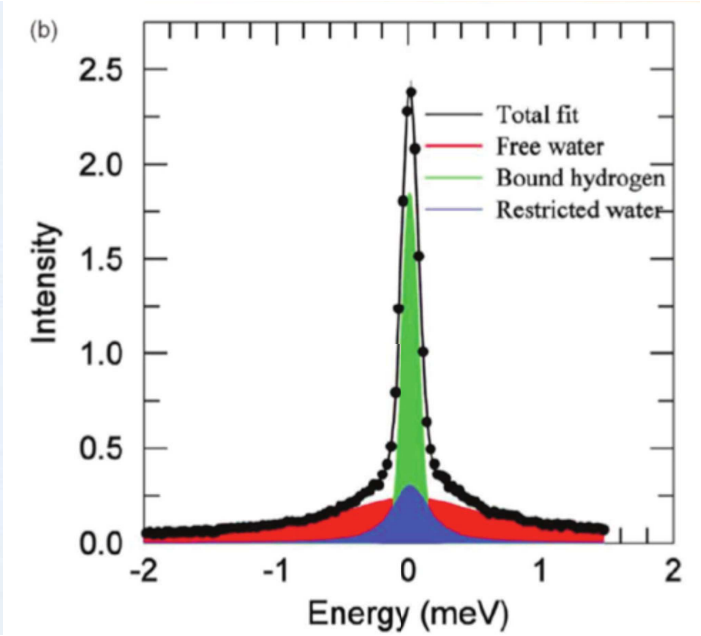

Figure 1.3: *The scattering function $S(Q,\omega)$ consists of different parts. The E part (green) will contain the signal from structurally bound hydrogen, and, in the particular case of H_2O, a hydrogen moving too slowly to be resolved in the investigated time-scale. The QE part of the signal is described by two Lorentzians, one for each observed water population. The narrow Lorentzian (blue) describes the signal from hydrogen in slow moving water that is somewhat restricted in the sample. The broad Lorentzian (red) describes the signal from the hydrogen in the fast moving free water. [25]*

tion; slow movement requires a narrow Lorentzian and fast motions require a broad Lorentzian, to describe the data. A detailed description of this analysis is given in Chapter 2.

The scattering function, $S(Q,\omega)$, is measured as a function of energy transfer, ω, between neutron and sample, and momentum transfer, Q. The width of the QE signal may change as a function of Q, as seen in the example in Figure 1.4 taken from [26]. In this experiment, the diffusive motions of water were studied as a function of temperature. The figure shows the measured $S(Q,\omega)$ at 5°C for three different values of Q. The Q-dependence of the QE width contains information about the type of motion as shown in Figure 1.5. Rotational motion gives rise to a QE contribution that is constant over Q, while translational diffusion can be seen by a linear dependence in Q^2.

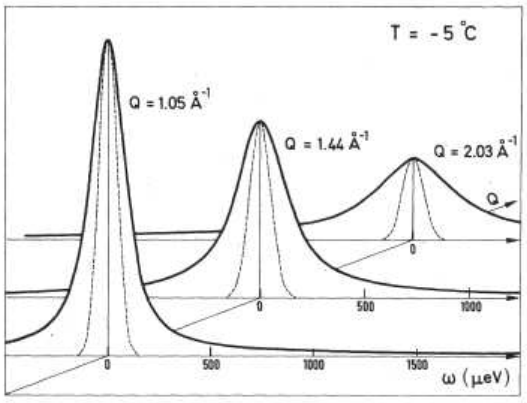

Figure 1.4: *Evolution of the Lorentzian width of the QE signal from water at $-5°$ C changes as a function of Q [26]. Copyright (1985) by The American Physical Society.*

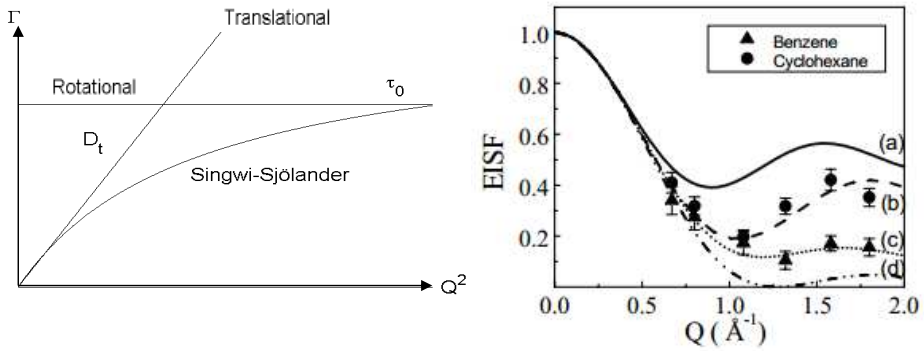

Figure 1.5: *(left) The Q^2-dependence of the Lorentzian widths contains information on the type of motion. Rotational diffusion is constant over Q^2 while translational diffusion is linear. The diffusion of bulk water can be modeled by the Singwi-Sjölander model. (right) The shape of the EISF as a function of Q contains information on the geometries of the confined motion. In this example taken from [27], the dynamics of Benzene and Cyclohexene adsorbed in HZSM-5 zeolite were studied: (d) is the theoretical EISF for isotropic rotational diffusion, while (a), (b) and (c) are for jumps among 2, 3 and 6 equivalent sites on a circle.*

Another important piece of information can be gained from the fraction of the elastic component contained within the whole signal. This fraction is called the elastic incoherent structure factor EISF, and was first formulated

by Lechner [28]. It is defined as:

$$\mathrm{EISF(Q)} = \frac{I^{el}(Q)}{I^{el}(Q) + I^{qe}(Q)}, \tag{1.2}$$

where I^{el} and I^{qe} are the integrals of elastic and quasi-elastic scattered intensities [24]. The Q-dependence of the EISF contains information on the geometry of the confined motion. Examples of this are shown in Figure 1.5.

To summarize, the scattering function, $S(Q, \omega)$, can be divided into distinct components, each associated with different proton motions. The subsequent analysis allows QENS to be used to study the mobility of the water in confinement, and more specifically here, water located in the cement pores. The nature of the mobility can be determined by analyzing the Q-dependence of the width of the QE signal, while the geometry of the motion can be determined by analyzing the EISF. Understanding of the different types of proton motions in different cements can then be linked to known structural-strength differences.

Chapter 2

Theoretical Aspects of Quasi-Elastic Neutron Scattering

When a neutron scattering experiment is conducted, in the most simplistic of terms, a beam of neutrons is applied to a sample to see what happens. When we know the state of the neutrons prior to hitting the sample and measure the state of the neutrons after hitting the sample, we can, by noticing the changes in neutron states, understand what happens in the sample. Of course, in reality this process is far more complicated, and to interpret what the changes in the neutron states mean, some theory is needed.

I will begin with some general comments about the properties of neutrons and the particle-wave duality of their description. This will be followed by a discussion of the energy transfer, ω, and momentum transfer, Q, which may occur when neutrons are scattered in the sample. Subsequently, the concepts of *scattering cross section* and *nuclear scattering length* will be explained, leading to the partial differential scattering cross section. The latter describes the measured quantity when neutrons are scattered from the sample, and its relation to the van Hove correlation functions through the scattering functions will be developed [29]. Here a differentiation between coherent and incoherent scattering will be made followed by an outline of the information that can be gained from the analysis of elastic (E), quasi-elastic (QE) and inelastic (IN) scattering from the sample. In our study, hydrogen will dominate the measured signal and we will focus on the E and QE response from the contributions. I will discuss the diffusion model that was used for analyzing the QE part of the data and explain how one can gain information from the E contribution.

2.1 Basic Properties of the Neutron

In order to better understand the theory behind neutron scattering some general concepts must be understood. Neutron scattering is an experimental technique where neutrons are used as probe to study the structure and dynamics of matter. A central part of quantum mechanics is the particle-wave duality, which postulates that particles can exhibit both particle and wave properties, depending on how they interact with their surroundings and are observed [30]. From a neutron scatterer's point of view, the appropriate description depends on what process of an experiment is being dealt with. When neutrons are created at the source, they are considered particles, their interaction with matter is described through wave mechanics and during their subsequent detection they are again considered particles. Free neutrons have a lifetime of just under 15 min and they decay into protons by a process known as beta decay through the emission of an electron and an electron anti neutrino [31]. As particles, neutrons have spin-1/2 with a mass of $m_n = 1.675 \cdot 10^{-27}$ kg and a magnetic moment $\mu = -1.913\ \mu_{\mathrm{N}}$.

The wave nature of neutrons is described through the de Broglie formalism. Neutrons moving with a velocity v can be described as waves with a wavelength λ:

$$\lambda = \frac{2\pi\hbar}{m_n v}, \tag{2.1}$$

where $\hbar = 6.582 \cdot 10^{-16}$ eV s^{-1} is the reduced Planck constant. The wavelength is related to the wave vector $\mathbf{k}$ by:

$$\lambda = \frac{2\pi}{|\mathbf{k}|} \qquad \text{where} \qquad \mathbf{k} = \frac{m_n}{\hbar}\mathbf{v}. \tag{2.2}$$

Traditionally in neutron scattering, wavelengths are given in units of Å (10^{-10} m) and wave vectors in Å^{-1}. Neutrons used in scattering experiments can be considered to move with non-relativistic speeds and the neutron kinetic energy is given by:

$$E = \frac{\hbar^2 k^2}{2m_n}, \tag{2.3}$$

which is measured in meV. The strength of neutrons as probes are multi fold. Low-energy neutrons are categorized as cold, thermal or hot according to their energy. While there is no standard definition of these ranges, cold and thermal neutrons can be considered to have wavelengths of $1 - 30$ Å and energies of $0.1 - 100$ meV. These are of the same order of magnitude as

those of excitations and inter-atomic distances in condensed matter. As a result, thermal and cold neutrons are ideally suited as probes for condensed matter [32].

Unlike X-rays, which interact electromagnetically with the electrons in a sample, neutrons interact with the nucleus. This interaction is random between elements and even between different isotopes of elements. One can therefore use neutrons to study light elements that are otherwise difficult to study with X-rays. The most distinct example being hydrogen, which is almost invisible to X-rays but highly visible to neutrons. The probability of interaction between X-rays or neutrons and the sample, is given by the cross section, which will be described in detail later. For most elements this interaction is relatively weak, a property which combined with the fact that neutrons have no electrical charge, allows neutrons to penetrate most matter easily [21]. Neutrons are typically able to penetrate several centimeters into metal, while X-rays will only penetrate a few micrometers or millimeters. For this reason neutrons probe the bulk of the sample and not just the surface. Samples can also be contained in various types of environments such as cryostats, pressure cells and furnaces.

As mentioned before, neutrons have a magnetic moment, this property combined with their ability to penetrate most matter and the fact that they interact with the nucleus of sample atoms, allows them to be used to probe the magnetic properties of a sample [21]. This however, will not be addressed further.

A final difference to be noted between X-rays and neutrons is the non-destructive effect neutrons have on a sample. Due to its ionizing nature, X-ray radiation can have a destructive effect on some systems. This effect is especially pronounced in biological systems subjected to highly energetic X-rays from synchrotron sources. The destructive effect from X-rays comes from two sources: the creation of free radicals or the destruction of molecular bonds within the sample [33]. Conversely, this is not observed when using neutrons.

2.2 Energy and Momentum Transfer in Scattering

The information obtained from using neutrons as probes comes from the analysis of energy and momentum changes in the neutron states before and after being scattered by the sample. Denoting the initial and final states of the neutron by the subscripts i and f respectively, the energy change in the *sample*, ΔE, is related to the energy change of the neutron and is given by:

$$\Delta E = \hbar\omega = E_i - E_f = \frac{\hbar^2}{2m_n}(k_i^2 - k_f^2). \tag{2.4}$$

The energy transfer between neutron and sample, ω, is given in units of s^{-1} and the multiplication by $\hbar$ ensures that ΔE is in units of energy (eV). The momentum change $\mathbf{Q}$ is given by:

$$\hbar\mathbf{Q} = \hbar(\mathbf{k}_i - \mathbf{k}_f), \tag{2.5}$$

where the sign convention is taken from [34]. Figure 2.1 shows a schematic of a neutron scattering experiment.

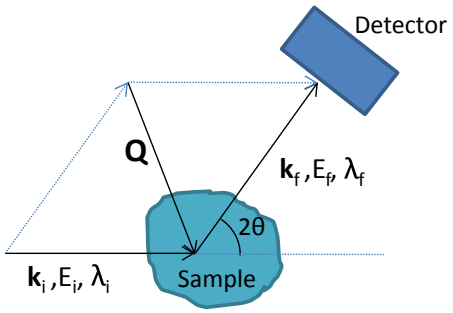

Figure 2.1: *The principles of a typical scattering experiment. Incident neutrons with wavelength λ_i, wave vector $\boldsymbol{k}_i$ and energy E_i are scattered in a sample. The neutrons are then detected at an angle 2θ with wavelength, wave vector and energy λ_f, $\boldsymbol{k}_f$ and E_f respectively. The momentum transfer $\boldsymbol{Q}$ is given by $\boldsymbol{Q} = \boldsymbol{k}_i - \boldsymbol{k}_f$.*

From an energy point of view, two types of scattering can take place: elastic and inelastic. These can be divided into three distinct cases:

- Inelastic scattering with $\hbar\omega < 0 \Rightarrow k_i < k_f$. Here energy is transferred from the sample to the neutron resulting in neutron energy gain.

- Elastic scattering with $\hbar\omega = 0 \Rightarrow k_f = k_i$. Here no energy is transferred between neutron and sample.
- Inelastic scattering with $\hbar\omega > 0 \Rightarrow k_i > k_f$. Here energy is transferred from the neutron to the sample resulting in neutron energy loss.

Figure 2.2 shows the scattering vector diagrams for these three cases.

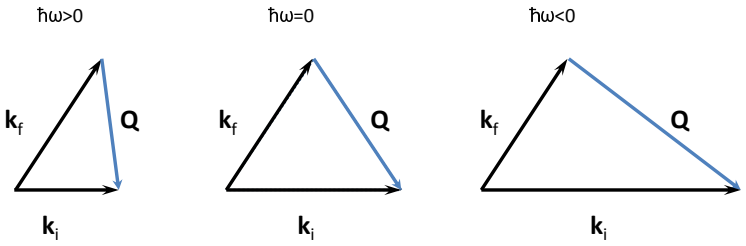

Figure 2.2: *Scattering vector diagrams for sample energy loss $\hbar\omega < 0$ with $k_i < k_f$, no energy change $\hbar\omega = 0$ with $k_i = k_f$ and sample energy gain $\hbar\omega > 0$ with $k_i > k_f$.*

In the case of inelastic neutron scattering a special case exists, and it is called quasi-elastic neutron scattering (QENS). This is inelastic neutron scattering with an energy change centered around $\omega = 0$.

An overview of the scattering types in relation to energy transfer is given in Figure 2.3. In this figure the dynamical structure factor, or scattering function, $S(Q, \omega)$, is shown as a function of change in sample energy, $\hbar\omega$. $S(Q, \omega)$ contains information on the intensity of the scattered neutrons, and will be described in further detail later. The elastic scattering is centered at $\omega = 0$. For positive ω inelastic scattering, the sample gains energy from the neutron through the creation of a phonon; in an analogy to Raman scattering, this is called the Stokes side of the energy spectrum. For negative ω inelastic scattering, the sample loses energy to the neutron, which in turn absorbs a phonon; this is called the anti-Stokes side [35].

At low temperatures, fewer excited states are occupied in the system compared to higher temperatures. Consequently, at lower temperatures fewer neutrons gain energy from the sample than loose energy to the sample. The scattering functions for neutron energy gain and loss are related through the principle of detailed balance [32]:

$$S(-Q, -\omega) = e^{-\hbar\omega/k_b T} S(Q, \omega). \tag{2.6}$$

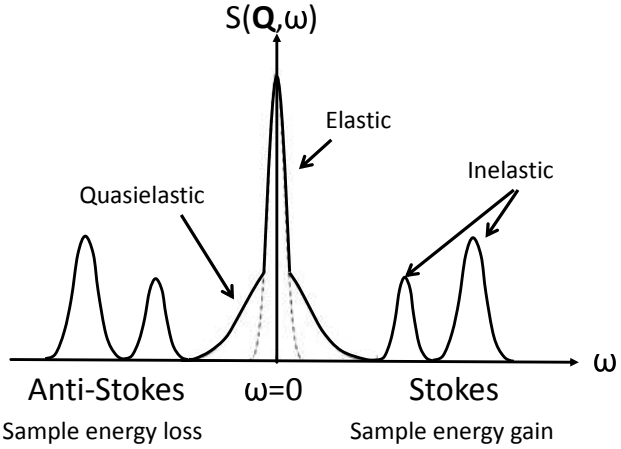

Figure 2.3: *Elastic and quasi-elastic scattering are both centered at $\omega = 0$. For positive ω the sample gains energy from the neutron by entering an excited state and creating a phonon, this is the Stokes side of the spectrum. For negative ω the sample loses energy to the neutron, which absorbs a phonon, this is the anti-Stokes side of the spectrum. The relative intensities are arbitrary.*

Examining the high temperature limit we see that:

$$T \to \infty \Rightarrow e^{-\hbar\omega/k_bT} \to 1, \tag{2.7}$$

which means that at high temperatures the scattering functions for sample energy gain and energy loss will approach an equal intensity. In the low temperature limit we see that:

$$T \to 0 \Rightarrow e^{-\hbar\omega/k_bT} \to \begin{cases} \infty & \text{for } \omega < 0 \\ 0 & \text{for } \omega > 0. \end{cases} \tag{2.8}$$

From this we see that, as the temperature decreases to a level where only ground states are occupied in the sample, the neutrons can no longer gain energy when scattering from the sample, resulting in the disappearance of the scattering function on the anti-Stokes side of the spectrum. This is illustrated in Figure 2.4, which shows the principle of detailed balance.

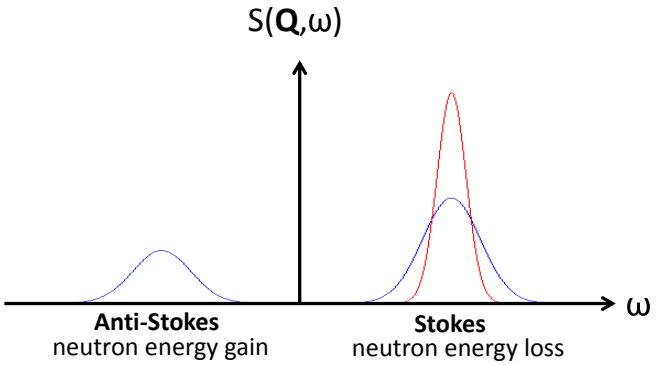

Figure 2.4: *For a temperature that is sufficiently high for excited states to be occupied in the sample, the scattering function is present in both the Stokes and the anti-Stokes side of the spectrum (blue signal). However as the temperature decreases to such a level where only ground states are occupied, neutrons can no longer gain energy when scattering in the sample. The scattering function on the anti-Stokes side of the spectrum therefore disappears (red signal). The signal on the Stokes side increases proportionally, as only the allowed values of ω changes with temperature and not the number of scattered neutrons.*

2.2.1 Scattering Examples

A. Inelastic Neutron Scattering

An example of a scattering experiment is given by Copley and Udovich in [36]. Figure 2.5 (left) shows the spectra for trimethylsilys adsorbates bonded to silica via surface oxygens. An energy loss feature at around 2.5 meV at 4 K shows up as both energy loss and energy gain features at 10 K due to the increasing population of the 2.5 meV level above the ground state as the temperature is raised. Figure 2.5 (right) shows elastic and inelastic scattering observed in a powdered sample of $HoPd_2Sn$. As the temperature of the system is increased, transitions from higher-energy levels to lower-energy levels are observed. ($E < 0$)

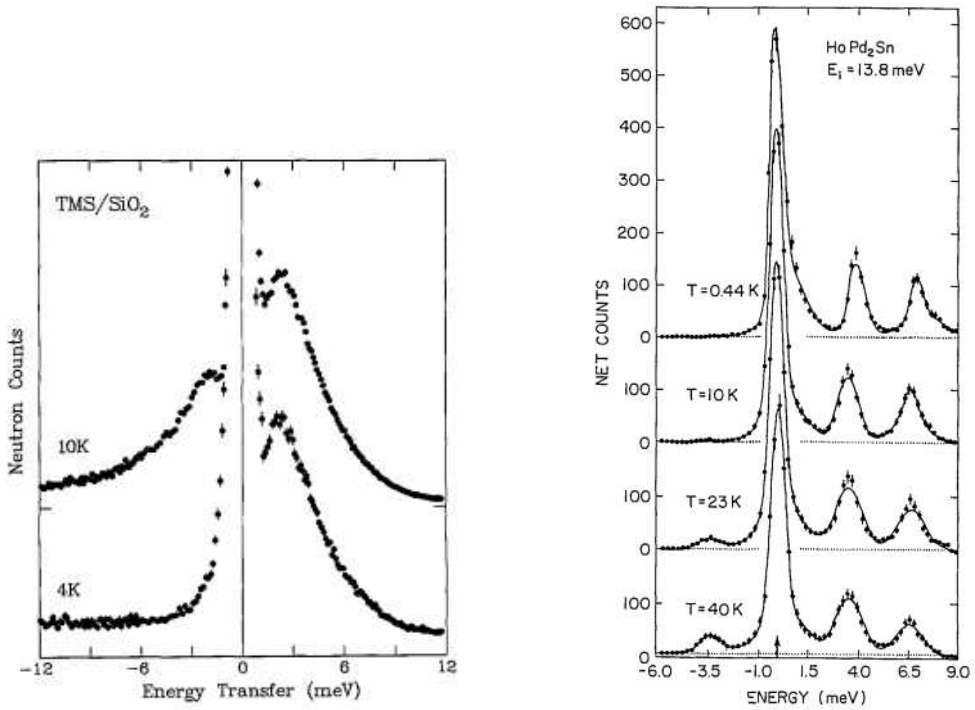

Figure 2.5: *(left) The spectra for trimethylsilys adsorbates bonded to silica via surface oxygens. An energy loss feature at around* 2.5 *meV at* 4 *K shows up as both energy loss and energy gain features at* 10 *K due to the increasing population of the* 2.5 *meV level above the ground state as the temperature is raised.[36]*

B. Quasi-Elastic Neutron Scattering

Another example is given by Teixeira et al. [26] who have studied the diffusive motions of water at low temperatures. They were able to super cool water and measure the QE spectra at nine different temperatures ranging from 20°C to −20°C. Measurements were done in the momentum transfer range $0.25 < Q < 2$ Å^{-1} and with an energy resolution of $\Delta E = 100$ μeV. Figure 2.6 (left) shows an example of how the QE signal for a given temperature changes for different values of Q. Figure 2.6 (right) shows the Q-dependence of the width of the QE signal for the nine different measured temperatures. By analyzing this Q-dependence for different temperatures, a separation between the rotational and translational motions of water molecules is possible.

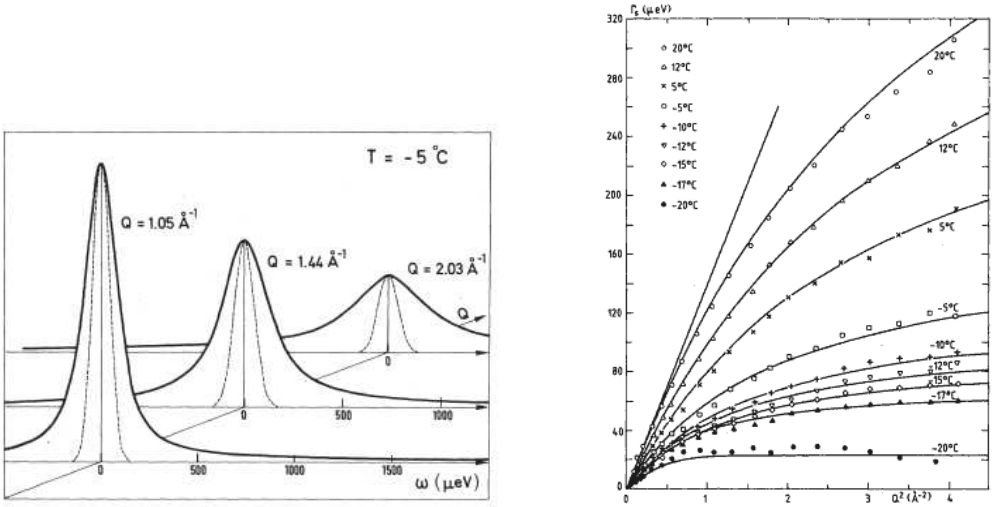

Figure 2.6: *(left) The measured QE spectra for water at $-5°C$ and a resolution of $\Delta E = 100$ meV. The width of the spectra is seen to change as a function of Q. (right) The Q dependent width of the QE signal for the measured temperature range [26]. Copyright (1985) by The American Physical Society.*

C. Elastic Fixed Window

A third example is given by Bordallo et al. [37]. In this experiment, the differences in water dynamics related to the presence of cations in two types of clay, montmorillonite and halloysite, is explored. To obtain an overall view of the water dynamics in the two clay types the elastic fixed window (EFW) technique was used. In this technique the structure factor $S_{elastic}(Q, \omega = 0)$ is measured as a function of temperature and can be related to the Debye-Waller factor,

$$S_{elastic}(Q, \omega \approx 0)(T) = e^{-\frac{1}{3}\langle u(T)^2 \rangle Q^2}. \tag{2.9}$$

As the temperature increases the elastic intensity decreases. A rapid decrease is the result of a sudden increase in the QE line width, indicating an activation of a motion in the time window of the instrument. The EFW measurements were carried out with three different resolutions. In Figure 2.7 the data has a summed Q-range between 0.4 Å and 1 Å and is normalized to unity at the lowest temperature. Rapid decrease in the elastic intensity is seen at various temperatures, allowing for the determination of the differences in the water dynamics in the two clays.

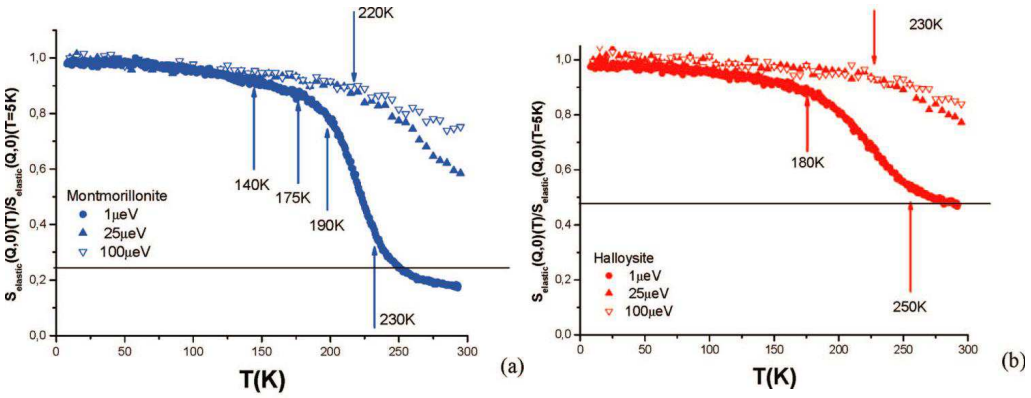

Figure 2.7: *Comparison between the normalized elastic intensities of montmorillonite (left) and halloysite (right) clay, at three different energy resolutions as a function of temperature. The horizontal lines indicate the ratio of hydrogen in hydroxyls to water. The arrows indicate inflection points where the decrease deviates rapidly from an approximately linear behavior. This is indicative of the onset of rotational or translational diffusion. Figure is reprinted with permission from [37]. Copyright (2008) American Chemical Society.*

In order to interpret the data in experiments such as these, one needs to understand some fundamental principles of neutron scattering. These will be discussed in the next section.

2.3 Mathematical Foundations of Neutron Scattering

2.3.1 Cross Section, Coherence and Incoherence

The possibility of statistical fluctuations affecting the results of a scattering experiment, is essentially dependent on counting rate. The precision and quality of a scattering experiment is directly connected to the number of neutrons scattered by a sample and subsequently detected, and therefore dependent on the strength of the neutron source [38]. The reactor at the Institute Laue-Langevin (ILL) in Grenoble is the most intense neutron

research reactor in the world. It generates $1.5 \cdot 10^{15}$ n/s/cm^2 in the moderator region. The flux on the sample is much smaller as many neutrons are lost on the way. This can, for example, happen in guides, choppers and monochromators. The flux on the sample at the cold neutron backscattering spectrometer IN10 is of the order of $0.5 - 4 \cdot 10^4$ n/s/cm^2 and a wavelength of 6.3 Å [39]. An alternative to the reactor production of neutrons is the spallation approach. In these sources, a pulsed proton beam releases neutrons from a target through a process called spallation. An example of a spallation source is the ISIS facility at the Rutherford Appleton Laboratory in the UK. The IRIS backscattering spectrometer at ISIS has an intensity on the sample of $1 \cdot 10^7$ n/s/cm^2 [40].

The flux of a neutron beam, Ψ, is defined as

$$\Psi = \frac{n}{s}, \tag{2.10}$$

where n is the number of neutrons impinging on a target surface per second and s is the surface area perpendicular to the neutron beam direction. Using Eq. (2.10) we can define the neutron scattering cross section, σ, as a systems ability to scatter neutrons:

$$\sigma = \frac{1}{\Psi}\text{number of neutrons scattered per second}, \tag{2.11}$$

σ has the dimensions of a surface, and is quoted in units of barn, 1 barn = 10^{-24} cm. If we consider that the neutrons are scattered in all directions, the surface area perpendicular to the neutron beam is the total solid angle 4π. The total scattering cross section can then be written as:

$$\sigma = 4\pi b^2, \tag{2.12}$$

where b is called the nuclear scattering length. In general the nuclear scattering length varies from nucleus to nucleus. This is due to variations of nuclear spin direction with time, differences between isotopes and elements. There is no *a priori* way of determining the nuclear scattering length and they are in general measured and tabulated. Values can for example be found in the Neutron Data Booklet [22].

As the scattering lengths vary between isotopes (isotope incoherence) and depend on the spin orientation of the nucleus relative to the neutron (spin incoherence) [21], the neutron does not see a uniform distribution of scattering potentials, but one that varies from point to point. It is only the average

scattering potential that can give rise to interference effects and thus coherent scattering. Then by assuming a random distribution of scattering lengths, the deviations from the mean are random and therefore cannot give rise to interference effects. The deviations from the mean thus give rise to incoherent scattering.

The incoherent scattering has been divided into two cases, spin incoherence and isotope incoherence. The first is due to the scattering length b being dependent of the relative spin orientations of the neutron and the nucleus. This effect is especially dominating in the case of hydrogen, H. For nuclei with zero nuclear spin this effect does not occur. This results in different isotopes having different scattering lengths and is the reason for isotope incoherence [21].

Figure 2.8 illustrates the relationship between total, coherent and incoherent scattering lengths. The coherent scattering length, b_{coh}, is the mean of the scattering lengths, $\langle b \rangle$, and is given by:

$$\langle b \rangle = \sum_i c_i b_i, \tag{2.13}$$

where c_i is the fractional concentration of nuclei with scattering length b_i. The corresponding scattering cross section is called the coherent scattering cross section:

$$\sigma_{coh} = 4\pi b_{coh}^2 = 4\pi \langle b \rangle^2 . \tag{2.14}$$

The incoherent scattering length, b_{inc}, is the deviation of the individual scattering lengths from the mean scattering length, and is given by:

$$b_{inc} = \sqrt{\langle b^2 \rangle - \langle b \rangle^2}. \tag{2.15}$$

This leads to the incoherent scattering cross section:

$$\sigma_{inc} = 4\pi b_{inc}^2 = 4\pi \left(\langle b^2 \rangle - \langle b \rangle^2 \right). \tag{2.16}$$

The total scattering length σ is the sum of the coherent and incoherent scattering lengths:

$$\sigma = \sigma_{coh} + \sigma_{inc}. \tag{2.17}$$

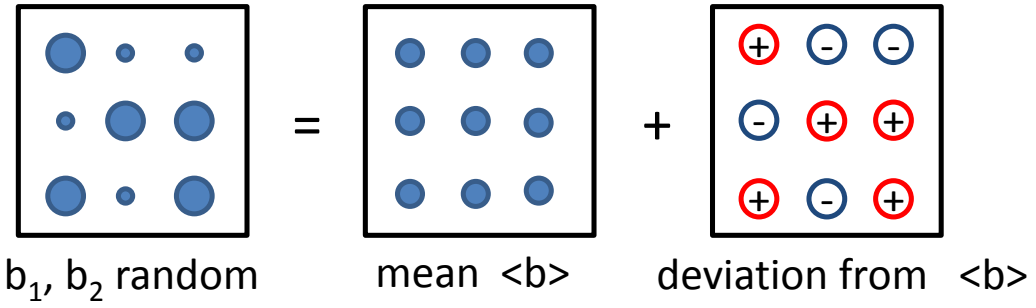

Figure 2.8: *We assume a random distribution of scattering lengths. For simplicity two different scattering lengths b_1 and b_2 are shown. The coherent scattering length, b_{coh}, is the mean of the two scattering lengths. The incoherent scattering length, b_{inc}, is the deviation of the individual scattering lengths from the mean. The total scattering length is seen as the sum of the coherent and incoherent scattering lengths.*

2.3.2 Partial Differential Scattering Cross Section

As it is not feasible to place detectors in the total solid angle, we are interested in the number of neutrons scattered into an element of the solid angle Ω, as shown in Figure 2.9. We are also interested in the energy transfer between sample and scattered neutrons, ω. The basic measured quantity in a scattering experiment is the partial differential scattering cross section $\partial^2\sigma/\partial\Omega\partial\omega$ [41]. When an experiment is conducted, the measured quantity is the intensity of scattered neutrons and this intensity is proportional to the partial differential scattering cross section. When an energy exchange between neutron and sample takes place, the intensity is given by:

$$dI = N\phi(\epsilon_i)\Delta\epsilon_i \frac{\partial^2\sigma}{\partial\Omega\partial\omega}\Delta\Omega\Delta\epsilon_f, \tag{2.18}$$

where N is the number of elements in the scattering volume, $\phi(\epsilon_i)$ is the neutron flux, $\Delta\epsilon_i$ is the incident neutron bandwidth, $\Delta\Omega$ is the collection solid angle and $\Delta\epsilon_f$ is the scattered neutron energy window. All these terms are fixed during the experiment as a result of instrument design and other factors such as the neutron source properties. Of importance here is that the partial differential scattering cross section can be separated into distinct coherent and incoherent parts [34], as seen in:

$$\boxed{\frac{\partial^2\sigma}{\partial\Omega\partial\omega} = \frac{\sigma_{coh}}{4\pi\hbar}\frac{\mathrm{k}_f}{\mathrm{k}_i}\mathrm{S}_{coh}(Q,\omega) + \frac{\sigma_{inc}}{4\pi\hbar}\frac{\mathrm{k}_f}{\mathrm{k}_i}S_{inc}(Q,\omega)} \tag{2.19}$$

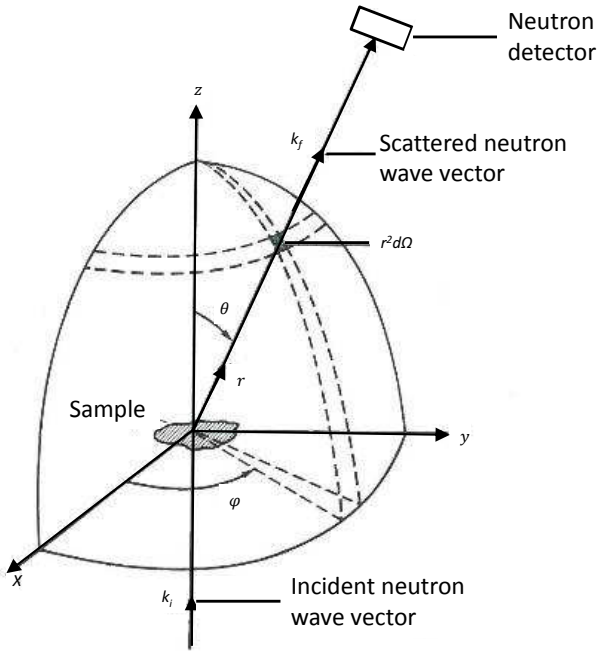

Figure 2.9: *The incident neutron is scattered by the sample into the solid angle element $r^2 d\Omega$. Figure is adapted from [21].*

$S_{coh}(Q,\omega)$ and $S_{inc}(Q,\omega)$ are the coherent and incoherent dynamical structure factors, or scattering functions. They are proportional to the measured intensity, and are essentially what is measured in an experiment. The actual derivation of Eq. (2.19) from Eq. (2.18) is given in Appendix A.

2.3.3 Dynamical Structure Factors and the van Hove Correlation Functions

It has been shown by van Hove [29] that the scattering of neutrons by an arbitrary system can be described by time-dependent distribution functions that correlate the positions of pairs of atoms. These so-called van Hove correlation functions are related to the scattering functions through Fourier transformations. The Fourier transformation of the van Hove correlation function $G(\mathbf{r},t)$ with respect to space yields the intermediate scattering function $I(Q,t)$, and a further Fourier transformation into the frequency domain yields the scattering functions, $S(Q,\omega)$.

As the correlation functions are functions of real time and space and not frequency and reciprocal space, their meaning is more easily interpreted. Van Hove's correlation function $G(\mathbf{r}, t)$ is explained by Vineyard [42], as the probability that, if an atom is at the origin at time 0, an atom will also be found within unit volume at position $\mathbf{r}$ at time t. It should be noted that the atom found at the origin does not need to be distinct from the one found later at $\mathbf{r}$.

Just as the total scattering function σ can be divided into two parts, so can van Hove's correlation function be divided into two parts: a distinct part and a self part. The distinct part $G_d(\mathbf{r}, t)$ gives the probability of finding at $\mathbf{r}$ and at time t an atom that is distinct from the one found at the origin at time 0; in this sense it deals with a pair of atoms and is therefore also called the pair correlation function. This probability distribution can, for example, be used to describe a phonon. Taking the 4-dimensional Fourier transformation of the distinct part yields the coherent scattering function $S_{coh}(Q, \omega)$. The self part $G_s(\mathbf{r}, t)$ gives the probability of finding at $\mathbf{r}$ and at time t the atom that was at origin at time 0. The self part describes the wandering of an atom away from some arbitrary starting point, and can be used to describe the diffusion of atoms [42]; its Fourier transform yields the incoherent scattering function $S_{inc}(Q, \omega)$.

As mentioned earlier, different elements have different coherent and incoherent scattering lengths. Table 2.1 shows the coherent and incoherent scattering lengths for the elements contained in cement.

Table 2.1: *Coherent and incoherent scattering lengths for thermal and cold neutrons of elements found in ordinary Portland cement and ashes. Values are found in [22] and units are barn* [$1barn = 10^{-24}cm^2$].

	H	C	O	Si	Ca	H_2O
σ_{coh}	1.76	5.55	4.23	2.16	2.78	7.75
σ_{inc}	80.26	0.001	0.00	0.004	0.05	160.52

From the hydration process shown in Eq. (1.1) we know that a significant amount of hydrogen is present in the cement, while from the values in Table 2.1 we see that the presence of hydrogen results in a σ_{inc} which is much larger than σ_{coh}. Consequently we will assume that the contribution from coherent scattering is negligible compared to the incoherent scattering

from hydrogen. As the experiments described herein are on cement, we will consider only the incoherent part of Eq. (2.19) and the self part, $G_s(\mathbf{r}, t)$, of the van Hove correlation function from now on.

The self part of the van Hove correlation function can be split into two parts [43]:

$$G_s(\mathbf{r}, t) = G_s(\mathbf{r}, \infty) + G'_s(\mathbf{r}, t), \tag{2.20}$$

where the first term is the value of the correlation function at very long times i.e. $t \to \infty$. Fourier transforming into intermediate scattering functions we have:

$$I_{inc}(Q, t) = I_{inc}(Q, \infty) + I_{inc}(Q, t), \tag{2.21}$$

where the intermediate scattering function is split into a time independent part and a time dependent part. Taking the Fourier transform we get:

$$S_{inc}(Q, \omega) = S^{el}_{inc}(Q, \infty)\delta(\omega) + S^{in}_{inc}(Q, \omega), \tag{2.22}$$

where the scattering function has now been separated into a purely elastic component and an inelastic component. For a particle diffusing in a volume that is effectively without boundary:

$$G_s(\mathbf{r}, \infty) = 0,$$

and consequently:

$$I_{inc}(\mathbf{r}, \infty) = 0.$$

As a result the elastic part of Eq. (2.22) will be absent.

Conversely, if the particle diffuses within a volume with a boundary then $G_s(\mathbf{r}, \infty)$ will have a finite value. This will give rise to a non-zero broadening of the elastic line in reciprocal space, as shown in Figure 2.10 (bottom). In the static case of an immobile atom, the probability of finding it at a certain position is constant in time; this gives rise to a δ-function in reciprocal space as shown in Figure 2.10 (top). The presence of a lattice structure will also give rise to an elastic scattering contribution, this scattering is however coherent, while the former is incoherent. Unless a separation between coherent and incoherent scattering is viable, the possibility of a significant coherent contribution to the elastic signal must be considered.

In the case where no coherent contributions to the elastic signal are present, an elastic part implies the presence of localized motion. This will be dealt with in more detail in Section 2.5. Taking the time-dependent Fourier transform of the time-dependent part of the intermediate scattering function Eq.

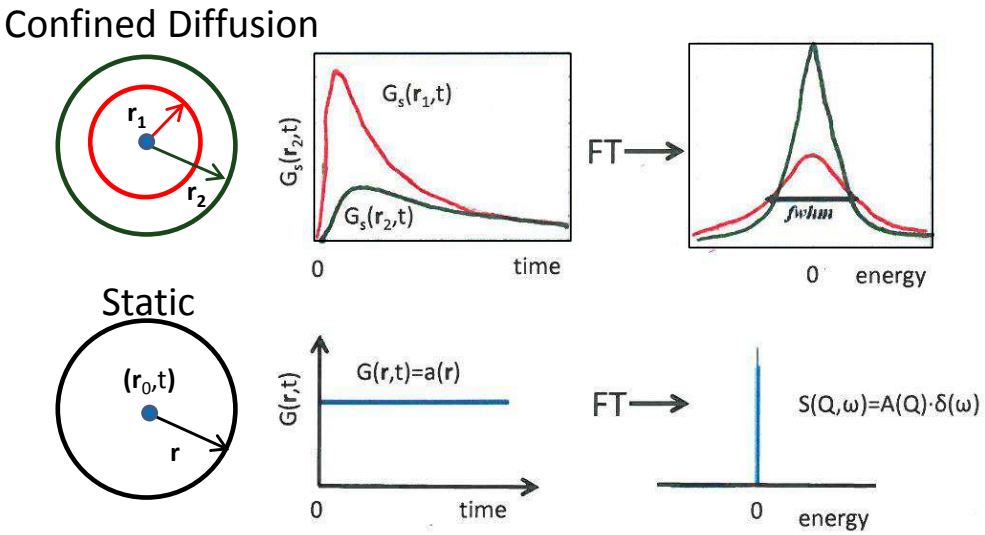

Figure 2.10: *In the case of an immobile atom, the probability to find it a certain position is constant in time. This probability corresponds to a δ-function in reciprocal space, $S(Q,\omega) = A(Q)\cdot\delta(\omega)$. In the case were an atom is bound to a finite volume, $G_s(\boldsymbol{r},t)$ approaches a finite value $G_s(\boldsymbol{r},\infty)$ for $\boldsymbol{r}$ varying in the interior of the volume. This results in a non-zero broadening of the elastic line in reciprocal space. The Figure is modified from [44].*

(2.21) results in a function with a non-vanishing broadening of the signal around $\omega = 0$ [45]. This broadening is the quasi-elastic scattering function, which contains information on the dynamical properties of the scatterers. From this separation in Eq. (2.22), we see why quasi-elastic neutron scattering contains information on both the structure and dynamics of the probed atoms.

A molecule will in general undergo several different types of motion at the same time. It can have internal vibrations, while rotating about itself and slowly moving through its surroundings. If these motions are happening in completely different time scales they can be considered decoupled. Their scattering functions can then be described independently of each other and the total scattering function is a convolution of the scattering functions attributed to each of the motions:

$$S_{inc}(Q,\omega) = S_{inc}^{Vibration}(Q,\omega) \otimes S_{inc}^{Translation}(Q,\omega) \otimes S_{inc}^{Rotation}(Q,\omega), \quad (2.23)$$

where the scattering functions associated with each of the three types of motion are described in the following section.

2.4 Scattering Functions of the Different Types of Motion

From Eq. (2.23), it is clear why the scattering of neutrons can be divided into several types, as shown in Figure 2.11. As already briefly discussed in section 2.2, this division can be separated into inelastic scattering with $\omega \neq 0$, quasi-elastic scattering with $\omega \approx 0$ and elastic scattering with $\omega = 0$, as well as a coherent and incoherent scattering.

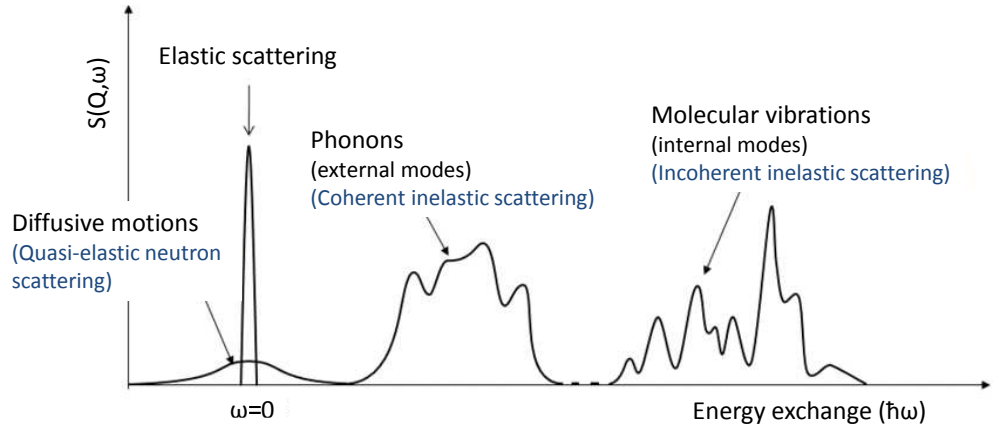

Figure 2.11: *Immobile scatterers give rise to an elastic signal, which contains information on the structure of the sample. Diffusive motions give rise to a quasi-elastic signal. Collective motions of the scatterers, such as phonons, give rise to a coherent inelastic signal. Uncoordinated random motions of the scatterer, such as internal molecular vibrations result in an incoherent inelastic signal. Image courtesy of ILL [39].*

Elastic scattering is observed when the neutrons do not exchange energy with the atoms in the sample. In the coherent case of elastic scattering, interference of the outgoing waves will take place, this gives rise to Bragg reflections and can be used to determine crystal structures [21]. If the elastic scattering is incoherent, no interference effects take place, and the associated elastic incoherent structure factor (EISF), which will be described in detail later, can be used to determine the geometries of the motions of the scattering atoms [45]. In elastic scattering experiments the structure factor $S(Q, \omega = 0)$ is the measured quantity.

Considering now the inelastic scattering, we can distinguish between coherent and incoherent origins of the signal. When the scattering atoms in the sample are mobile, they will give rise to an inelastic or quasi-elastic signal [46]. This signal will be coherent if the motions in the sample are collective, phonons for example. If the scattering atoms in the sample move in an uncoordinated fashion at random, the scattering signal will be incoherent. An example of incoherent inelastic scattering is molecular vibrations where the scattering atoms are vibrating within a molecular structure, but the individual molecules vibrate independently of each other. An example of this is the vibration of the OH bond in water. The last type of scattering is the quasi-elastic scattering. Here the energy exchange between sample and neutron is small (hence the name quasi-elastic) and centered on the elastic signal. Quasi-elastic scattering originates in small motions of atoms in the sample, such as diffusion, hydrogen rotations in methyl groups or tunneling effects.

2.4.1 Vibrational Motions and the Debye-Waller Factor

The vibrational motions of molecules can be separated in three types:

- Internal molecular vibrations where the atoms in the molecule are in periodic motion, continuously stretching or bending their bonds.
- External librations where the molecule with a nearly fixed orientation rotates slightly back and forth.
- External translational vibrations where the molecule with a nearly fixed position translates back and forth.

The scattering functions related to the internal molecular vibrations $S^V_{inc}(Q,\omega)$ and the external vibrations and librations of the whole molecule $S^L_{inc}(Q,\omega)$, can be separated into an elastic part and an inelastic part [45]:

$$S^V_{inc}(Q,\omega) = e^{-\frac{1}{3}\langle u^2_V\rangle Q^2}\left[\delta(\omega) + S^V_{in}(Q,\omega)\right] \quad (2.24)$$

$$S^L_{inc}(Q,\omega) = e^{-\frac{1}{3}\langle u^2_L\rangle Q^2}\left[\delta(\omega) + S^L_{in}(Q,\omega)\right], \quad (2.25)$$

where the first term is the Debye-Waller factor. $\langle u^2_V\rangle$ and $\langle u^2_L\rangle$ are the mean-square displacements of the atom. $S^V_{in}(Q,\omega)$ is composed of a series of inelastic spectral lines related to the vibrational levels of the molecule,

these are however of the order 100 meV and have no influence in the QE region of interest. $S_{in}^{L}(Q,\omega)$ is a slowly varying term, which in the QE region takes the form of a small background [45]. The result is that the convolution Eq. (2.23) takes the form:

$$S_{inc}(Q,\omega) = e^{-\frac{1}{3}\langle u^2\rangle Q^2}\left[S_{inc}^{Translation}(Q,\omega) \otimes S_{inc}^{Rotation}(Q,\omega) + S_{inc}^{I}(Q,\omega)\right], \tag{2.26}$$

where the first term is the Debye-Waller factor and

$$\langle u^2\rangle = \langle u_V^2\rangle + \langle u_L^2\rangle \tag{2.27}$$

is the mean-square displacement of the atom under the effects of internal and external modes. In the QE region the Debye-Waller factor accounts for the effects of vibrations. Outside this region the inelastic term $S_{inc}^{I}(Q,\omega)$ accounts for the vibrations. It is well known from thermodynamics that the mean-square displacement of the atom about its equilibrium position increases with temperature. The Debye-Waller factor and its temperature dependent effect on the elastic intensity is derived in Appendix B.

2.4.2 Rotational and Translational motion

The scattering function describing rotational motion was derived by Sears [47] in 1966. In this model the rotational motion is assumed to be confined on the surface of a sphere with radius a, and is described by the Sears expansion:

$$S_r(Q,\omega) = j_0^2(Qa)\delta(\omega) + \frac{1}{\pi}\sum_{l=1}^{\infty}(2l+1)j_l^2(Qa)\frac{l(l+1)D_r}{\omega^2 + (l(l+1)D_r)^2} \tag{2.28}$$

where D_r is the rotational diffusion coefficient, characterized by a relaxation time $\tau_r = \frac{1}{6D_r}$ and j_l are the spherical Bessel functions. The Sears expansion is essentially an infinite series of Lorentzians with Q-independent half-widths at half maximum (HWHM) $\Gamma = l(l+1)D_r$. Figure 2.12 shows the first five terms of the Sears expansion. As not all Bessel functions will contribute to the signal over the entire Q-range accessible at an instrument, the Sears expansion can be approximated to a finite series of Lorentzians. In practice the scattering function describing rotational motion can be approximated to that of a single Lorentzian [49].

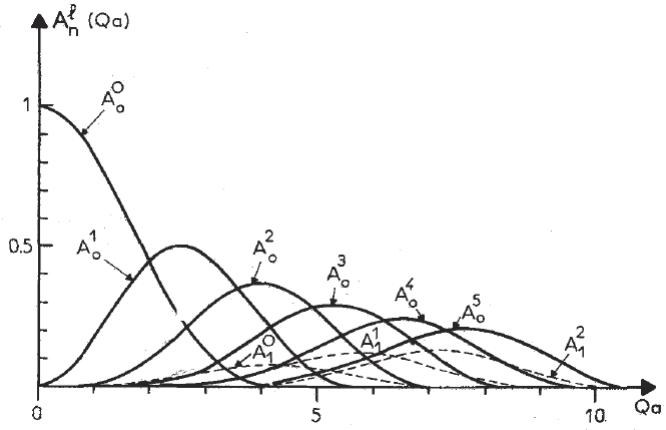

Figure 2.12: *The first five terms of Eq. (2.28). As seen not all terms contribute to the signal over the entire Q-range. In practice, no instrument can access all of Q and as a result the Sears expansion can always be approximated to a finite series of Lorentzians. Figure is from [48]*

One of the simplest forms of translational diffusion is that of Brownian motion where the particles move under the influence of the forces that arise from their mutual collisions [45]. This motion is governed by the translational diffusion constant D_t, which can be described through the Einstein relation:

$$D_t = \frac{\langle l^2 \rangle}{6\tau_t}, \tag{2.29}$$

where the particle travels a distance l during the time τ_t. The translational diffusion commonly modeled by Brownian motion leads to the following scattering law derived by Vineyard [42]:

$$S_t(Q,\omega) = \frac{1}{\pi} \frac{D_t Q^2}{\omega^2 + (D_t Q^2)^2}. \tag{2.30}$$

The shape of this function is Lorentzian with a Q-dependent half-width at half maximum (HWHM), Γ, given by:

$$\Gamma = D_t Q^2, \tag{2.31}$$

and centered in $\omega = 0$. The Q-dependence of the translational and rotational half-widths Γ are shown in Figure 2.13 (left).

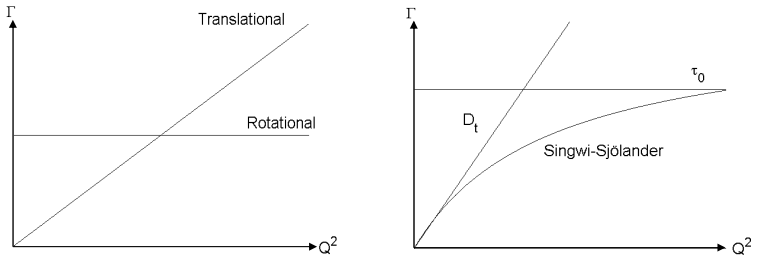

Figure 2.13: *(left) The Lorentzian HWHM of the rotational motion is Q-independent. The translational diffusion is given by the D_tQ^2 law. (right) The Singwi-Sjölander model describes the diffusion of bulk water. For low Q it approaches the D_tQ^2 law and for high Q it asymptotically approaches a plateau given by the relaxation time τ_0.*

2.4.3 The Diffusional Motion of Bulk Water

In the case of *bulk water* this simple D_tQ^2 dependence has proven insufficient to accurately describe the diffusion of *bulk water*, especially at high Q [50]. It was suggested that molecular motions in liquid water occurs by finite jumps, and a jump model was developed by Singwi and Sjölander [51]. In this model the water molecule oscillates for a time τ_0 before diffusing a distance l over the time period τ_1. In the limiting case $\tau_1 \gg \tau_0$ the Singwi-Sjölander model reduces to the expression derived by Vineyard, Eq. (2.30). In the case of $\tau_1 \ll \tau_0$ it instead takes the form of a Lorentzian with a HWHM shown in Figure 2.13 (right) and given by:

$$\Gamma_t = \frac{D_tQ^2}{1 + D_tQ^2\tau_0} \qquad \text{with} \qquad D_t = \frac{L^2}{6\tau_0}. \tag{2.32}$$

This is the well-known Singwi-Sjölander jump diffusion model. As the time the molecule translates is much shorter than the time spent oscillating, the model can be seen to describe a molecule spending time τ_0 at a given position and then jumping a mean distance L to a new site. It should be noted that in the low Q limit Eq.(2.32) reduces to the D_tQ^2 law and in the high Q limit it approaches $\frac{1}{\tau_0}$. Using this model, the temperature dependent diffusive properties of water have been thoroughly investigated both in bulk and confinement [26], [49].

2.5 The Case of Confinement

We now have the tools necessary to construct a scattering function that describes the temperature dependent scattering from *confined water*. Considering Eq.(2.23), we know from section 2.4.2 that rotational and translational motions can be described by Lorentzians. In the case of water these motions can be combined in a quasi-elastic scattering function, whose shape is a Lorentzian, described by the Singwi-Sjölander model. From Eq.(2.22) we know that an elastic component is introduced when the water is confined. Due to a variety of factors such as analyzer mosaicity, backscattering angle and the characteristics of the neutron source, the energy resolution of an instrument is not a δ-function [34]. Therefore the scattering function must be convoluted with the known resolution function of the instrument $R(Q,\omega)$. And at last we know from section 2.4.1 that the intensity of the signal is affected by the Debye-Waller factor. Putting all this together, the total incoherent scattering function Eq.(2.23) now becomes [52]:

$$S\left(Q,\omega\right) = e^{-\frac{1}{3}\left\langle u(T)^2\right\rangle Q^2}\left[\left(A_0(Q)\delta(\omega) + (1-A_0)(Q)L\left(\Gamma,\omega\right)\right) \otimes R(Q,\omega)\right] + B(Q), \tag{2.33}$$

where the first term is the Debye-Waller factor which takes into account the effects of vibrational motions in the quasi-elastic region, $R(Q,\omega)$ is the resolution of the instrument, $B(Q)$ is a possible background and the quasi-elastic scattering is described by a Lorentzian L with half-width at half maximum (HWHM) Γ. The Q-dependence of Γ will give indications on the type of motion observed in the experiment. In the case of *bulk water* Γ can, and will in this thesis, be modeled using the Singwi-Sjölander model, Eq. (2.32).

As explained in Section 2.3.3, the coefficient $A_0(Q)$ of the delta function is a space-Fourier transform of the "infinite time" distribution in space i.e. the final position of all scattering nuclei averaged over all possible initial positions. It is called the elastic incoherent structure factor, EISF [53]. This is essentially the time averaged spatial distribution of the scatterers. If the scatterer is located in a space effectively without boundary, it is able to move infinitely far away in an infinite amount of time and thus the EISF is zero. If the scatterer is confined in some volume, there is a finite probability of finding it after an infinite amount of time, resulting in a non-zero EISF.

The Q-dependence of the EISF yields information on geometry of the scatterers motion. Small Q-values correspond to large volumes and vice versa. If the EISF approaches unity in the low Q limit, the scatterers are confined in some volume and not allowed to diffuse over long distances (corresponding to low Q-values). In the large Q limit, the EISF will approach zero if all scatterers are mobile, but will approach a non-zero value if some scatterers are immobile. If discrimination between the elastic and quasi-elastic parts of the peak is possible determination of the EISF is given by the relation:

$$EISF = \frac{I^{el}}{I^{el} + I^{qe}}, \tag{2.34}$$

where I^{el} and I^{qe} are the integrated intensities of the elastic and quasi-elastic parts of the peak.

The model described in Eq. (2.33) assumes that all the observed diffusive motions can be described by a single Lorentzian. It is quite possible that several different populations of protons are present in the sample, each subject to different translational and rotational constraints and with different motional properties. The Lorentzian in the scattering function is then a superposition of Lorentzians, each describing their own proton population. If a distinction between these populations is possible a single Lorentzian will not fit the data properly and a scattering function with more than one Lorentzian will be necessary [24], [54]. This leads to the following scattering function:

$$S\left(Q,\omega\right) = e^{-\frac{1}{3}\left\langle u(T)^2\right\rangle Q^2}\left[\left(A_0(Q)\delta(\omega) + \sum^{i} A_i(Q)L_i\left(\Gamma_i,\omega\right)\right) \otimes R(Q,\omega)\right] + B(Q), \tag{2.35}$$

where A_0 is the EISF, A_i are called the quasi-elastic incoherent structure factors (QISF), $R(q,\omega)$ is the resolution function of the instrument and $B(Q)$ is a possible background. Each distinguishable population of hydrogen is described by an associated Lorentzian $L_i(\Gamma_i,\omega)$.

Chapter 3

Experimental Aspects of Quasi-Elastic Neutron Scattering

While Chapter 2 dealt with the theoretical aspects of neutron scattering this chapter will describe the experimental aspects of the thesis. Section 3.1 explains the backscattering technique and describes the backscattering instruments IN10 located at the ILL, Grenoble, France and IRIS located at the ISIS facility, Rutherford Appleton Laboratory in the UK. This is followed by a section on the green cement experiment and another on the dental cement hydration experiment. These sections describe the sample preparations and how the experiments were carried out. Furthermore, they describe the steps needed to reduce the data prior to the analysis and also explain the methods used in such analysis.

3.1 Backscattering Spectroscopy

As outlined in previous chapters, neutron scattering is ideally suited to study the dynamic processes of hydrogen. A wide range of instruments and experimental techniques are available, and suited for the study of different dynamical motions. The choice of instrument depends completely on the information one wishes to gain, as shown in Figure 3.1. This figure shows a comparison of the different time-, length-, and energy ($\hbar\omega$)- scales accessed by neutron instruments. The momentum transfer range for backscattering instruments goes from 0.07 Å^{-1} at DNA at J-Parc [55] to 4.9 Å^{-1} at IN13 at ILL [56]. In addition to the accessible Q-range, energy resolution is of key importance, as this determines the time-scale of the observable dynamical

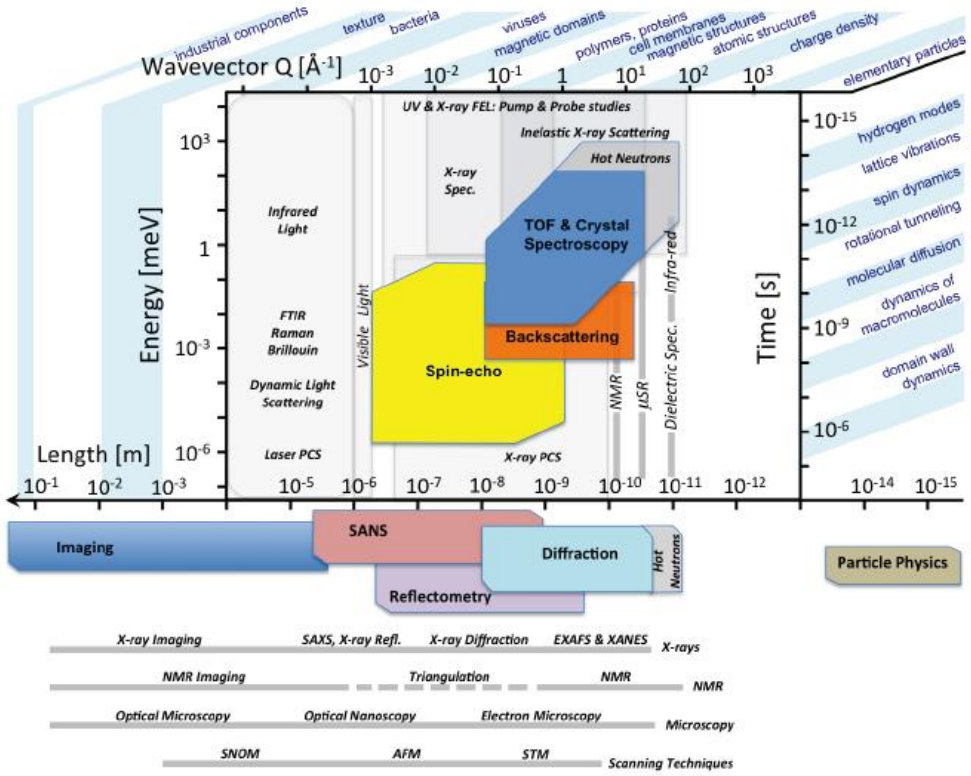

Figure 3.1: *Schematic plot illustrating the (Q, ω) range accessed by different spectroscopic techniques. Backscattering is seen to access a Q-range of $0.07 - 4.9$ $\AA^{-1}$ and motions on the ns and ps time scales [57].*

motions through the following relation [58]:

$$\Delta(\hbar\omega)\Delta t_{obs} \cong 2 \cdot \hbar, \tag{3.1}$$

where $\Delta(\hbar\omega)$ is the FWHM of the instrument energy resolution, Δt_{obs} is the observed time-range and $\hbar$ is the reduced Planck constant. The time-scale accessed by backscattering is seen in Figure 3.1 to be in the picosecond (ps) to nanosecond (ns) range. Table 3.1 shows the energy resolution and accessed time scale of the IRIS and IN10 backscattering spectrometers in the setup used for this study. The reasons for the choice of these instruments will be detailed in sections 3.2 and 3.3.

Table 3.1: *Experimental setup used for IN10 and IRIS.*

	$\Delta(\hbar\omega)(\mu$ eV)	Δt_{obs}(ps)	Q(Å^{-1})
IRIS	17.5	38	0.42 - 1.85
IN10	1	660	0.07 - 2.0

Backscattering spectrometers are indirect geometry spectrometers that measure an intensity proportional to the scattering function $S(Q,\omega)$. The momentum change Q is measured as a function of scattering angle. The energy change in the sample ΔE is measured indirectly, keeping the final energy E_f fixed and varying the incoming energy E_i about this value. Figure 3.2 [59] shows the energy transfer range accessible through direct and indirect geometry set-ups.

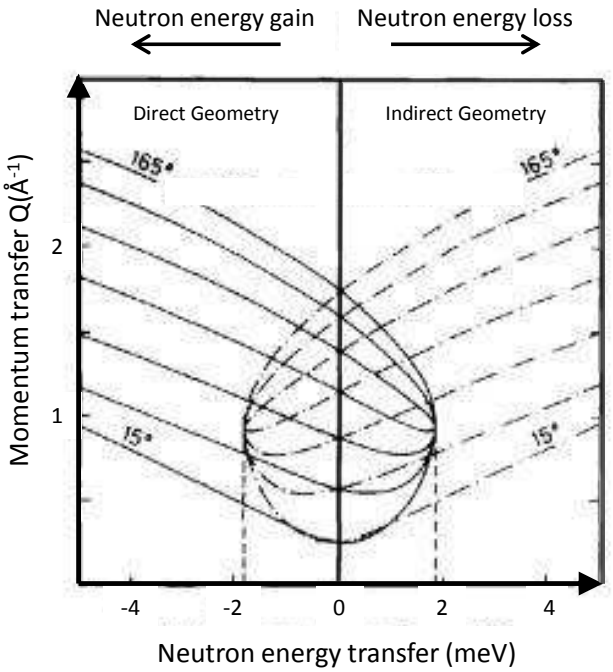

Figure 3.2: *Direct and indirect (inverted) geometry setups access different neutron energy transfer ranges [59].*

IN10 is located at the ILL in Grenoble. The neutron source at ILL is a reactor that continuously produces neutrons through fission. As a result, all wavelengths of neutrons continuously arrive at the instrument. IRIS, however, is located at the ISIS facility in the UK, where neutrons are produced

via the spallation process. Here neutrons are produced by pulses of high energy protons bombarding a tungsten target, thereby driving neutrons out of the nuclei. Contrary to the continuous distribution of the reactor-produced neutrons, spallation sources produce neutrons with an inherent variation in energy of the incident neutrons. The neutrons, therefore, arrive at the instrument in short pulses with the fastest, or most energetic and lower wavelength neutrons, in the beginning of the pulse, and the slower, or less energetic and longer wavelength neutrons, in the end of the pulse.

This difference in the arriving neutrons results in slightly different setups of the backscattering instruments depending on the neutron source. In the case of a reactor source, the incoming energy is monochromatized through backscattering and the energy varied about the chosen value by the doppler effect. The spallation source instrument instead uses time-of-flight to monochromatize the incident energy.

3.1.1 IN10

Figure 3.3 illustrates the high resolution nearly perfect backscattering spectrometer IN10. The Si(111) monochromator selects neutrons with a wavelength and energy of 6.271 Å and 2.080 meV and with an energy resolution width of 1 μeV at full-width at half maximum (FWHM). By using the same Si(111) reflection for the analyzers, the final and initial energies are the same. When the doppler drive is turned off, the incident energy on the sample does not vary. In this way only elastic measurements, such as elastic fixed window scans, are possible. By turning the doppler drive on, the monochromator moves rapidly back and forth and shifts the energies of the reflected neutrons through the doppler effect. In this way the initial energy is varied by 0.015 meV about the final energy. Only those neutrons whose energy change by the doppler drive match their energy transference to the sample, are reflected by the analyzers. Since the total distance from monochromator to detector is known exactly, every time channel belongs to a specific sample energy change ΔE.

The flux of neutrons produced by the Si(111) monochromator, is the same irrespective of whether the doppler is on or not. The energy distribution is however not the same, since activation of the doppler drive spreads the neutrons out over different energy ranges, thereby broadening the energy distribution of the backscattered neutrons. Since the flux distribution at the

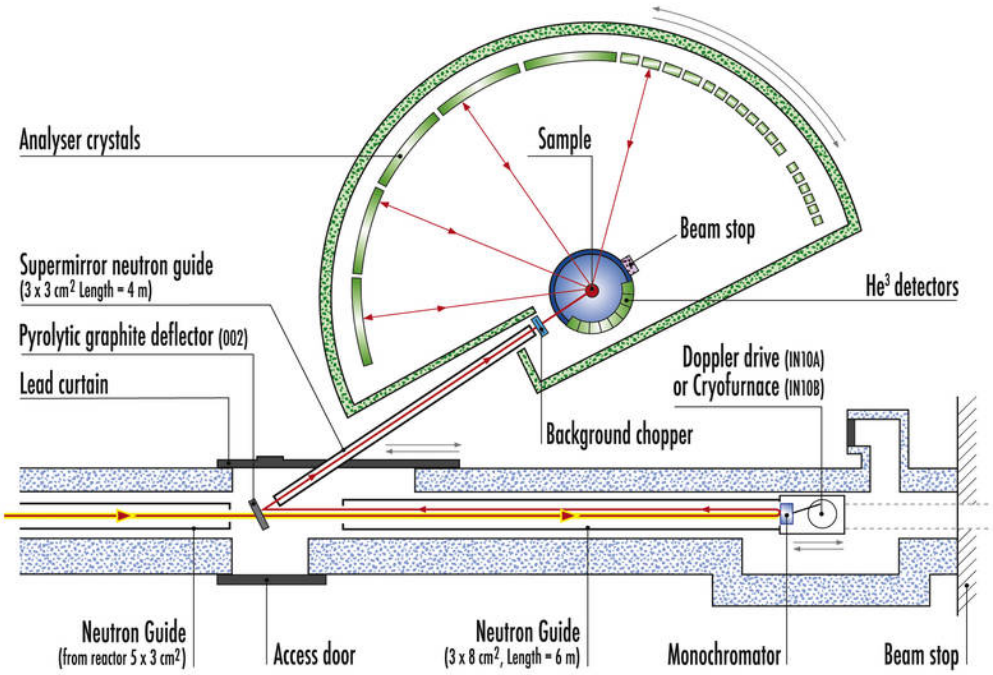

Figure 3.3: *Schematic of the IN10 backscattering spectrometer at the ILL reactor source. A cold neutron beam with a spectral distribution around 6 Å travels along a straight neutron guide section. The neutrons are then backscattered from a Si(111) monochromator mounted on a doppler drive. About 40% of the neutrons are then deflected into a second guide by a (002) oriented graphite crystal situated just below the primary beam. They travel trough a chopper that reduces background and onto the sample. The neutrons are scattered from the sample and backscattered onto 7 He^3 detectors by a series of Si(111) analyzers [60]. Image courtesy of ILL [60].*

sample remains the same, this causes a decrease in the intensity of elastically scattered neutrons, when the doppler drive is turned on. Therefore, the elastic intensity will be lower in a QENS measurement with the doppler on, than in an elastic measurement with the doppler off.

3.1.2 IRIS

Figure 3.4 illustrates the IRIS backscattering spectrometer. Here the incident neutrons are monochromatized by time-of-flight. The spallation source produces neutrons that travel toward the instrument in pulses. The neutrons pass through two disk choppers that prevent the slowest neutrons in a pulse from hitting the detectors at the same time as the fastest neutrons in the following pulse. The choppers rotate in such a way that the initial energy E_i is varied around the analyzing energy E_f [59]. For the ash and dental cement experiments the PG(002) offset setup was used. Here the final energy E_f selected by the graphite analyzers is 1.84 meV and the chopper rotation allows for initial energies spread unevenly about this value. In this setup the ΔE range is from -0.3 meV to 1.2 meV with an energy resolution width of 17.5 μeV (FWHM). After passing through the choppers, the neutrons pass through a monitor and hit the sample. The scattered neutrons are analyzed by 50 graphite analyzers covering scattering angles from 25° to 160° and located 85 cm from the sample. This corresponds to a Q-range coverage of 0.42 Å^{-1} to 1.85 Å^{-1} [61]. The analyzed neutrons are then backscattered at an angle of 175° below the horizontal plane onto a series of detectors. The total distance traversed by the detected neutrons from the choppers to the detectors is known precisely. This allows for the allotment of every time channel to a specific sample energy change ΔE.

3.2 The Construction Cement Experiment

Two construction cements, OPC and M700, were investigated with elastic incoherent neutron scattering (EINS) and quasi-elastic neutron scattering (QENS) using the IRIS backscattering spectrometer at ISIS. The results are summarized in Chapter 4.

By means of nuclear magnetic resonance (NMR) three types of proton mobility have been identified in hardened cements [62]–[64]. These mobilities were associated with the hydrogen in different water populations:

1. *Bound water* consisting of structural hydrogen in OH or H_2O water molecules chemically bound to solid phases in the C-S-H structure.
2. *Confined water* divided into:

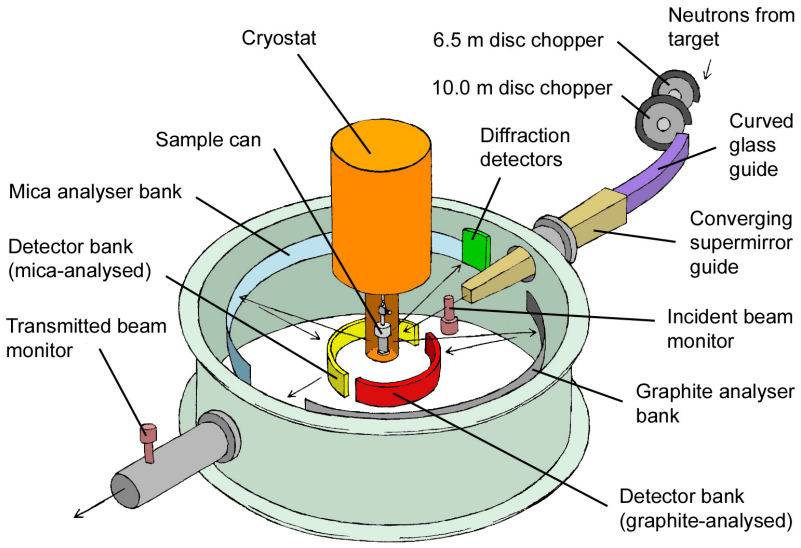

Figure 3.4: *Schematic of the IRIS high resolution inelastic spectrometer at the ISIS facility [40]. The neutrons pass through two choppers that select the desired neutron energy range. After passing through a monitor the neutrons are scattered from the sample. The neutrons are then backscattered onto detectors by a series of PG(002) analyzers. Image courtesy of ISIS [40].*

(a) Water which is confined in the smaller gel pores and exhibits a dynamic behavior similar to super-cooled *bulk water*; it is termed *glass-like* [65].
(b) Water which is confined in the larger capillary pores and behaves like constrained *bulk water*; it is termed *bulk-like*.

In the measurements described in Section 3.2.3, the structural hydrogen will contribute to the elastic signal while the hydrogen in the *confined water* populations, 2(a) and 2(b), will give rise to clear QE broadenings of the elastic signal.

After the initial mixing of the cement the structure matures gradually over time through hydration; the pore structure evolves and more and more dry cement gel forms. Figure 3.5 shows the volume fraction of unhydrated cement, dry gel, gel pores and capillary pores as a function of hydration. After 28 days, 75% of the hydration process has taken place. Since the capillary pores dominate the cement structure early in the process, it is

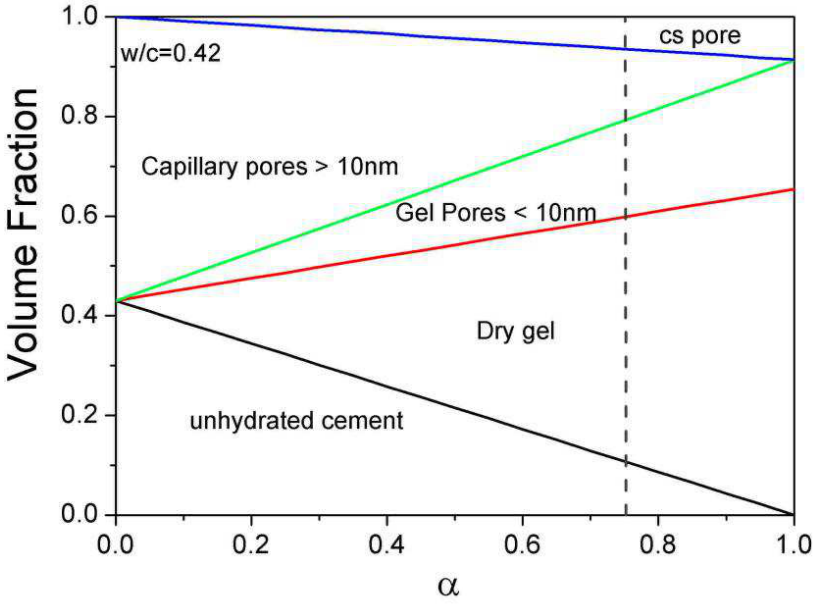

Figure 3.5: *Hydration of ordinary Portland cement. α defines the degree of hydration. The vertical dotted line indicates α after 28 days. As the hydration process slows down over time complete hydration at $\alpha = 1.0$ is never achieved. Figure is adapted with permission from [66]*

expected that investigations of cement much younger than 28 days will yield little evidence of *glass-like* water. Studying matured cement aged around 28 days will likely show the presence of both *bulk-like* water and *glass-like* water.

The three types of proton mobility identified by NMR in cement have been shown by QENS to occur on different time-scales. Bordallo et al. [67] found that *bound water* dynamics occur on a time scale much slower than the ps time-scale. This is supported by Hall et al., who studied interlamellar water in clays. They found that H bound to the clay is immobile on a time scale of $100 - 0.1$ ps [68]. Fratini et al. studied the evolution of water in the hydration process of cement [65]. They also determined by means of QENS that with a resolution of 28 μeV (a few tens of ps time-scale) only one type of mobile water was discernible. In addition, they observed that *bound water* was immobile in this time scale. In a similar hydration QENS study by

Fitzgerald et al., it was found that *bulk-like* water dynamics occur on the hundreds of ps time scale [69]. Accordingly on a ps time-scale *bound water* is seen as immobile, while *bulk-like* and *glass-like* water can be observed.

In our study of cement paste, the proton motion of interest was that of the constrained *glass-like* water. For this reason we wanted an instrument resolution which allows for a clear separation between the three types of proton motion. Therefore the IRIS high resolution backscattering spectrometer was chosen.

3.2.1 Sample Preparation

The two construction cement pastes were prepared by Michelle S. Rodrigues at the School of Agricultural Engineering FEAGRI, UNICAMP, São Paulo Brazil. The OPC sample was ordinary Portland cement prepared with a water to cement ratio by weight of 0.45 and allowed to mature for 28 days. The M700 sample was a blend by weight of 80% cement and 20% sugarcane bagasse ash burnt at 700°, also prepared with a water to cement ratio of 0.45 and matured for 28 days. Both samples were ground to a fine powder in a mortar and pestle, packed in aluminum foil packets and mounted in flat aluminum sample holders sealed with indium wire. Part of the samples were

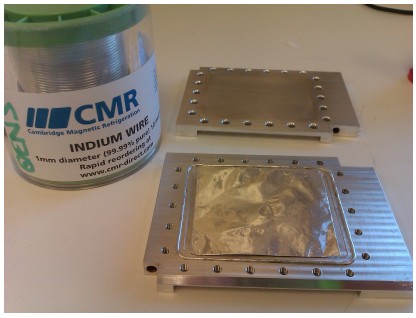

Figure 3.6: *The powdered cement paste was packed in an aluminum saché and mounted in a flat aluminum sample holder. The sample holder was sealed with indium wire and closed with* 22 *aluminum screws.*

dried in an oven at 110°. This temperature allows for the removal of the *confined water* without destroying the cement structure [67]. The samples were weighed at regular intervals, and when the weight no longer changed

over time, all the *confined water* was considered to have been removed. These two dried samples were mounted in the same way as the two hydrated samples described above. All four samples were weighed prior to being mounted in sample holders, and after they had been measured the samples were removed from the sample holders and weighed again to ensure that no water was lost during the measurements.

3.2.2 Elastic Incoherent Neutron Scattering Measurements

Elastic incoherent neutron scattering (EINS) experiments measure the structure factor, or elastic scattering factor, $S(Q, \omega = 0)$. Since the energy resolution has a finite width, the actually measured scattering function is $S(Q, \omega \approx 0)$. The elastic fixed window technique (EFW) is a type of EINS experiment that provides an overall view of the hydrogen dynamics as a function of temperature. This method measures the scattering function $S_{elastic}(Q, \omega \approx 0)$ as a function of temperature and relates it to the Debye-Waller factor previously explained in Section 2.4.1:

$$S_{elastic}(Q, \omega \approx 0)(T) = e^{-\frac{1}{3}\left\langle u(T)^2 \right\rangle Q^2}, \tag{3.2}$$

where $\langle u(T)^2 \rangle$ is the mean square displacement (MSD) of the molecule from its equilibrium position.

The change in intensity as a function of temperature contains information on the types of motion in the sample. At low temperatures the molecules are immobile and all signal is elastic. As the temperature increases they will begin to oscillate about their equilibrium positions, increasing the MSD and thus lowering the elastic signal. The change in elastic intensity can be described by a harmonic model, which is roughly linear. If however, rotational and translational motions are allowed, the change will deviate from a harmonic model. In this case the temperature will at some point have increased sufficiently for the molecules to begin rotating, and as the temperature is increased further, the unbound molecules will be able to translate through the system. The onset of these two motions will be seen by the appearance of a quasi-elastic broadening of the elastic signal and a subsequent sudden deviation from the harmonic decrease in elastic intensity. Furthermore, by considering the Q-dependence of the EFW, additional information can be gained as rotations contribute to the signal above 1 Å^{-1} and translations

below 1 $Å^{-1}$. Therefore the EFW technique enables an identification of the types of motion in the system and their activation temperatures. By comparing the elastic intensity at 5 K with the elastic intensity at 300 K, it is possible to determine the fraction of hydrogen which is bound in the sample at room temperature in the time-window probed by the instrument. A comparison of this fraction from the two cement pastes will reveal if the diffusivity of the protons are different in the two cements.

EFW scans were done on hydrated as well as dried OPC and M700. The samples were cooled down to 5 K, where all motion within the sample effectively ceased. The temperature was increased in interval steps of 5 K up to 300 K and data was collected for 7 min at each step. Each EFW scan thus has 96 data points. The angle between the plane of the sample and the incident beam was 135°. Because of this orientation, the 14 highest scattering angle detectors were shielded by the edge of the sample holder.

3.2.3 Quasi-elastic Neutron Scattering (QENS) Spectra Measurements

As explained in Chapter 2, diffusional motion causes a QE broadening of the elastic signal. The Q-dependence of this broadening allows for the determination of the diffusion coefficient and the relaxation time. In addition, the analysis of the QENS spectra is also needed to extract the EISF, which gives information on the spacial restriction of the diffusion process.

The QENS spectra for each of the four samples was measured at 300 K and 5 K. As no motion is present in the sample at 5 K, and all signal was contained in the elastic peak, these measurements were used to determine the resolution of the instrument for the given sample. The 300 K QENS measurements contained the signal from both the mobile and immobile hydrogen on the investigated time-scale. The hydrated samples contained signal from hydrogen in the *bound* and *confined* (*glass-like* and *bulk-like*) water populations. In the dried samples the *confined water* had been removed so the signal was only from the structural hydrogen in the *bound water* population. By subtracting the dried data sets from the hydrated ones, a data set containing only signal from the *confined water* was created for each of the two cement pastes.

Like the EINS measurements, the angle between the plane of the sample and the incident beam was 135°. Because of this orientation, the 14 highest scattering angle detectors were shielded by the edge of the sample holder.

3.2.4 Data Reduction

When the data is saved during the measurements, it is not saved in a readily accessible format, and before the analysis starts a careful data reduction is necessary. The data reduction was done using the MODES program available from the ISIS web page [70] following the instructions in the user guide [71]. The raw data is saved in a binary time-of-flight format in .raw files. Converting from time-of-flight .raw files to energy transfer .ipg files requires several steps. First a calibration file has to be created for each sample using the 5 K QENS measurements and the Calib routine in MODES. This routine reads the raw data file and calculates the area of the elastic peak for each spectrum. The Ionian routine is then used together with the calibration file to convert from time-of-flight to energy transfer, creating an .ipg file for each measurement. In this process, the calibration file created from the 5 K measurement is used to account for detector efficiency, and in addition the data is normalized to monitor count. When creating the .ipg files it is possible to sum the data from all 50 detectors together or divide them into groups of one or more detectors. Due to the sample orientation in relation to the incident beam, it was seen when looking at the signal from the detectors individually that the last 14 detectors had been shielded by the edge of the sample holder. The 14 detectors were therefore not included in the creation of the .ipg files.

EINS Data Reduction

For the EINS measurements, the data was summed in two detector groups. The first group contained all detectors corresponding to momentum transfer Q interval $0.442 - 0.998$ Å^{-1} and $\langle Q_1 \rangle = 0.525$ Å^{-1}, where translational motions dominate. In the second group, corresponding to Q interval $1.034 - 1.648$ Å^{-1} and $\langle Q_2 \rangle = 1.556$ Å^{-1}, the rotational motions dominate. The Elwin routine in MODES was then used to determine the integrated elastic intensity as a function of temperature. For each of the four samples, the 96 associated .ipg files were read and integrated within the sample resolution.

The result is an .elf file for each sample. These files contain the integrated elastic intensity within instrument energy resolution for all 96 temperature increments and are used to plot the EFW results in Chapter 4.

QENS Data Reduction

The QENS data was summed in 25 groups of 2 detectors each and the last 7 groups were discarded due to the shielding. In order to subtract the hydrated sample data sets from the dried ones, the Analyse routine was used. Using this routine, we subtracted the dried .ipg files from the hydrated .ipg files. The result was .ipg files containing only the signal from the *confined water* in the two cement types. The resulting two .ipg files, one for M700 and one for OPC, were exported to .dasc format to be analyzed using the DAVE program [72]. The Q-dependent QENS spectra were fitted in DAVE and the EISF and diffusion properties was obtained for each sample. The results are shown and discussed in Chapter 4.

3.3 Dental Cement Hydration

As explained in Section 1.2, understanding the hydration process during the setting of glass ionomer cements is the key to understanding the strength of the material. The hydration process of two dental restorative glass ionomer cements (pastes) (GIC) *Aqua Ionofil Plus* (AQUA) and *Ionofil Molar* (POLY) were investigated at IRIS as well as IN10 at ILL. In the POLY sample the polyacid is part of the liquid component, while in the AQUA sample it is incorporated in a freeze-dried state in the powder and the liquid used is water.

The GIC setting process undergoes several stages. When the dental cement paste is freshly prepared it has not yet started setting; it is malleable and easily applied to the cavity. The initial setting period lasts about 5 minutes, after which the material can no longer be molded. The hydration process then continues for several days and even weeks. During all these stages the material is highly sensitive to water sorption and dehydration. As the

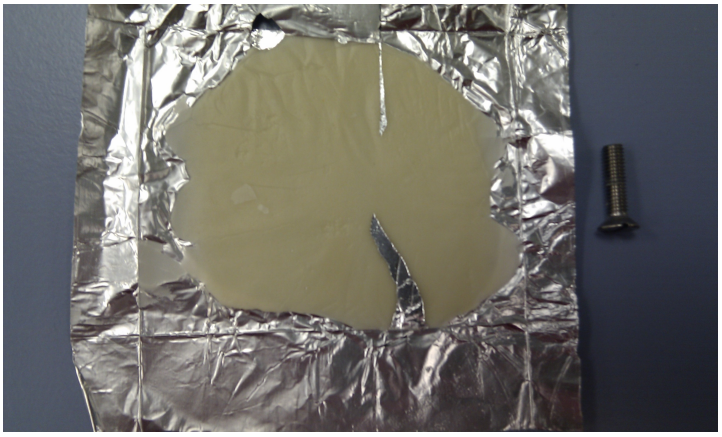

Figure 3.7: *Dental cement sample in aluminum saché, opened after the experiment was finished.*

cement matures, more and more hydrogen becomes chemically bound within the sample. By measuring the scattering function $S(Q, \omega)$ over time, this maturation is reflected by the increase of the elastic intensity.

3.3.1 Sample Preparation

The procedure for preparing the AQUA and POLY samples for the measurements were identical for the IN10 and IRIS experiments. The dried cement powders and liquid components were placed on a clean mixing surface. The components were then mixed together as quickly and thoroughly as possible before being placed on the aluminum foil, which was carefully weighed in the beginning of the procedure. The cement was sealed in the foil and rolled flat using a heavy steel rolling pin. The sample and aluminum saché were weighed and the weight of the foil saché subtracted to deduce the sample mass. The foil with the sample was then placed in the flat aluminum sample holder and sealed with indium wire. The sample holder was then mounted in the instrument and data collection initiated approximately 15 min after mixing had begun. Figure 3.7 shows a dental cement sample in its aluminum saché, opened after the experiment was finished.

Table 3.2 shows the time passed from sample preparation began until measurements were initialized.

Table 3.2: *Initialization time for hydration measurements at IN10 and IRIS.*

	AQUA	POLY
IRIS	16 min	15 min
IN10	14 min	18 min

3.3.2 Hydration Measurements

The samples were measured at 310 K, which corresponds to body temperature and a data point was collected every 15 min on IRIS and every 5 min on IN10. After 24 hrs the samples were removed from the cryostat and allowed to maturate in an oven set to 310 K, for 4 days in the IN10 experiment and 5 days in the IRIS experiment.

After the maturation period the sample was placed in the cryostat and measured again. After the final measurement the samples were weighed again to ensure that no liquid was lost during the experiments.

On IRIS and IN10 the samples were mounted so that the angle between the plane of the sample and the incident beam was 135°. In the IRIS experiment this resulted in the 14 highest scattering angle detectors being shielded by the edge of the sample holder. On IN10 the last two of the 7 detectors were shielded by the sample holder.

The main difference between the hydration measurements at IRIS and IN10 stems from the manner in which the instruments function. On IRIS the elastic and QE signals are measured at the same time. However on IN10, as explained in Section 3.1.1, one chooses whether to measure the elastic or the QE signal. The elastic signal is measured with the doppler drive turned off while the QE signal requires the doppler drive to be turned on. As explained in Section 3.1.1 the flux distribution is different for the two settings.

On IN10 the 24 hydration experiments were carried out with the doppler turned off to maximize the elastic flux since we were interested in the change in elastic intensity. The measurement of the matured samples after 4 days, was carried out with the doppler drive turned on to measure the QE signal, and off to measure the elastic signal.

For both the IRIS and the IN10 measurements, the QE signal is needed to determine the fraction of elastic signal contained within the total signal (elastic+QE). This defines the immobile hydrogen index which is explained in Section 3.3.3.

On both IRIS and IN10 a vanadium sample was measured, to normalize for detector efficiency. Furthermore, on IN10 an empty sample holder was measured, the spectrum from this is subtracted from the cement spectra. This reduces the noise in the analyzed data set as all background signal from the instrument and the sample holder is removed by subtraction.

3.3.3 Data Reduction

The data collected at IRIS was treated using MODES in much the same manner as the construction cement data. A vanadium sample was also measured to create the calibration files needed to correct for detector efficiency. The .ipg files were created using vanadium calibration files and all detectors except the 14 shielded ones were added together in one group. Two .elf files were created using the Elwin routine in MODES. The first file contains the integrated intensity of the total signal, between -0.3 meV to 1.8 meV, while the second contains only the integrated elastic intensity over the instrument resolution range. Dividing the elastic intensity by the total intensity provides the immobile hydrogen index (IHI),

$$\mathrm{IHI} = \frac{\text{elastic intensity}}{\text{total intensity}}. \tag{3.3}$$

In concrete hydration studies the immobile hydrogen index is also known as the *bound water* index (BWI) [73].

The data collected at IN10 was treated using MATLAB procedures (time scans) and the LAMP software package [74] (inelastic measurements). All measurements were normalized to the monitor count, as well as the vanadium measurement to account for any variation in detector efficiency. The empty sample holder measurements were subtracted from the resulting data sets. For the two 24 hour hydration measurements obtained on IN10 routines were then used to transform the data into sets containing the integrated elastic intensity as a function of 5 min time increments. The same routines were used to derive the elastic intensity after 4 days, from measurements done on the 4 day old samples, with the doppler drive off. The

total intensity was found by integrating the QENS signal from measurements taken of the 4 day old samples with the doppler drive engaged, using LAMP.

Like the IRIS measurements, the IHI from the IN10 measurements was found using Eq. (3.3). However, because the flux on the sample is different in an elastic and inelastic scan on IN10, a flux normalization is required. This means determining how much larger the flux is in the elastic part of the signal, when the doppler drive is off compared to when it is on. The width of the elastic signal was determined from a resolution measurement of the samples taken at 2 K, this width was then used to integrate the elastic part of the total intensity, yielding the elastic fraction of the QENS signal. This elastic fraction was then divided by the integrated elastic intensity of the 4 days old elastic measurement, resulting in the required normalization factor. The IHI is then normalized to the flux by dividing with this factor.

The time index for the measurements was adjusted to take the values in Table 3.2 into account, as well as the duration of each measuring point. In this way for example, the IHI for AQUA measured at IRIS and shown in Figure 5.1, begins at 31 min, with step sizes of 15 min. The IHI as a function of time indicates the degree of hydration [75]. These results are shown and discussed in Chapter 5.

Chapter 4

Neutrons Reveal Why Greener Cements Function Better

This chapter presents the results of the experiment described in Section 3.2. The elastic fixed window (EFW) results will be presented first. From these results we were able to identify two water populations in each sample. This is followed by an analysis of the quasi-elastic scattering results, here the diffusional motions of the identified water populations are presented together with the EISF results. Subsequently the results are discussed, a conclusion of the experiment will be presented together with the implications of our results.

4.1 Results

4.1.1 Elastic Incoherent Neutron Scattering

The temperature dependent structure factors, $S(Q, \omega = 0)$, obtained from the EINS measurements of the OPC and M700 cement pastes with $w/c = 0.45$, using the EFW approach are presented in Figure 4.1. Sub-figure 4.1(a) shows the hydrated OPC, 4.1(b) the hydrated M700, 4.1(c) the dried OPC and 4.1(d) the dried M700. All four sub-figures show $S(Q, \omega \approx 0)$ for $\langle Q_1 \rangle = 0.525$ Å^{-1} and $\langle Q_2 \rangle = 1.556$ Å^{-1} momentum transfer. For all four cement pastes $S(Q, \omega \approx 0)$ has been normalized to the lowest temperature.

As expected, due to the Debye-Waller factor, the elastic intensity $S(Q, \omega \approx 0)$ decreases as the temperature increases. The arrows point to inflection points due to an anomalous deviation from the harmonic decrease in elastic intensity. The deviation is related to the onset of diffusive motion that is faster than the instrument time resolution of about 150 ps. For both OPC

and M700 deviations are seen at 200 K and 250 K for $\langle Q_1 \rangle$ and again at 190 K and 240 K for $\langle Q_2 \rangle$. This is in agreement with previous hydrated cement paste studies [10], [76].

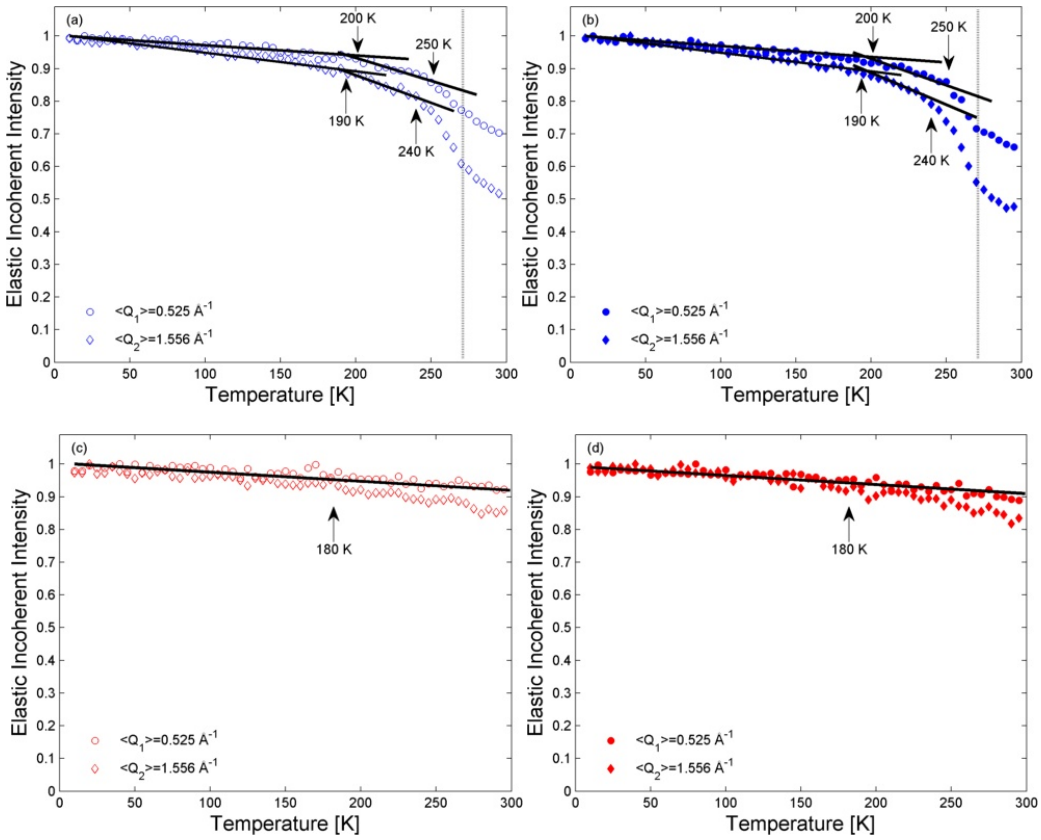

Figure 4.1: *Elastic fixed window scans of dried and hydrated OPC and M700 obtained using IRIS with $\Delta E = 17.5\ \mu eV$. Detectors have been summed in two groups with $\langle Q_1 \rangle = 0.525\ \AA^{-1}$ and $\langle Q_2 \rangle = 1.556\ \AA^{-1}$: (a) hydrated OPC cement paste; (b) hydrated M700 cement paste; (c) dried OPC cement paste; and, (d) dried M700 cement paste. The arrows mark the temperatures at which diffusive motions are activated. At 300 K the intensity is greater for the OPC cement than the M700 cement.*

Through the onset of these diffusive motions we can identify the *glass-like* and *bulk-like* water populations that we expect to find in the hydrated samples (see Section 3.2).

The inflection point at 190 K for $\langle Q_2 \rangle = 1.556$ Å^{-1} indicates the onset of rotational motion and the inflection point at 200 K for $\langle Q_1 \rangle = 0.525$ Å^{-1} indicates the onset of translational motion. This implies the presence of a water population in the hydrated cement that is confined in micro-pores and has a lowered transition temperature. We identify this water with the expected *glass-like* water confined in the gel-pores. This interpretation agrees with Takamuku et al. [77] who showed that by confining water in micro-pores of 3 nm the transition temperature can be lowered to 228 K.

Furthermore, Teixeira et al. [26] have shown that *bulk water* can be super cooled to 260 K before freezing. Thus, the inflection point at 240 K for $\langle Q_2 \rangle = 1.556$ Å^{-1} can be related to the onset of a second rotational motion and the inflection point at 250 K for $\langle Q_1 \rangle = 0.525$ Å^{-1} to the onset of a second translational motion. This evidences the presence of a second water population which we can identify with the expected *bulk-like* water.

Moreover the dotted horizontal line at 270 K indicates a third inflection point in the two hydrated samples. This implies that the samples contain some water which is truly *bulk water* and not confined within the sample, but most likely attached to its surface.

For the dried samples (4.1(c) and 4.1(d)) we see an inflection point around 180 K for $\langle Q_2 \rangle = 1.556$ Å^{-1}. A similar result has been reported in clays [78] and this motion was attributed to the activation of OH-rotations. This is indicative of OH groups bound to the surface of the pore structure.

The elastic intensity at 300 K is slightly higher in the OPC sample than the M700 sample, in both the dried and hydrated cases. Hence we can conclude that the OPC has less mobile hydrogen at 300 K and 28 days of age than M700, indicating that the hydration process is slower in M700 compared to OPC.

4.1.2 Quasi-Elastic Neutron Scattering

As described in Section 3.2.4, the QENS spectra were measured for hydrated and dried OPC and M700. Each spectrum was divided into 18 separate spectra with Q-values ranging from $Q = 0.46$ Å^{-1} to $Q = 1.62$ Å^{-1}. Examples of typical spectra are shown in Figure 4.2. Blue indicates hydrated

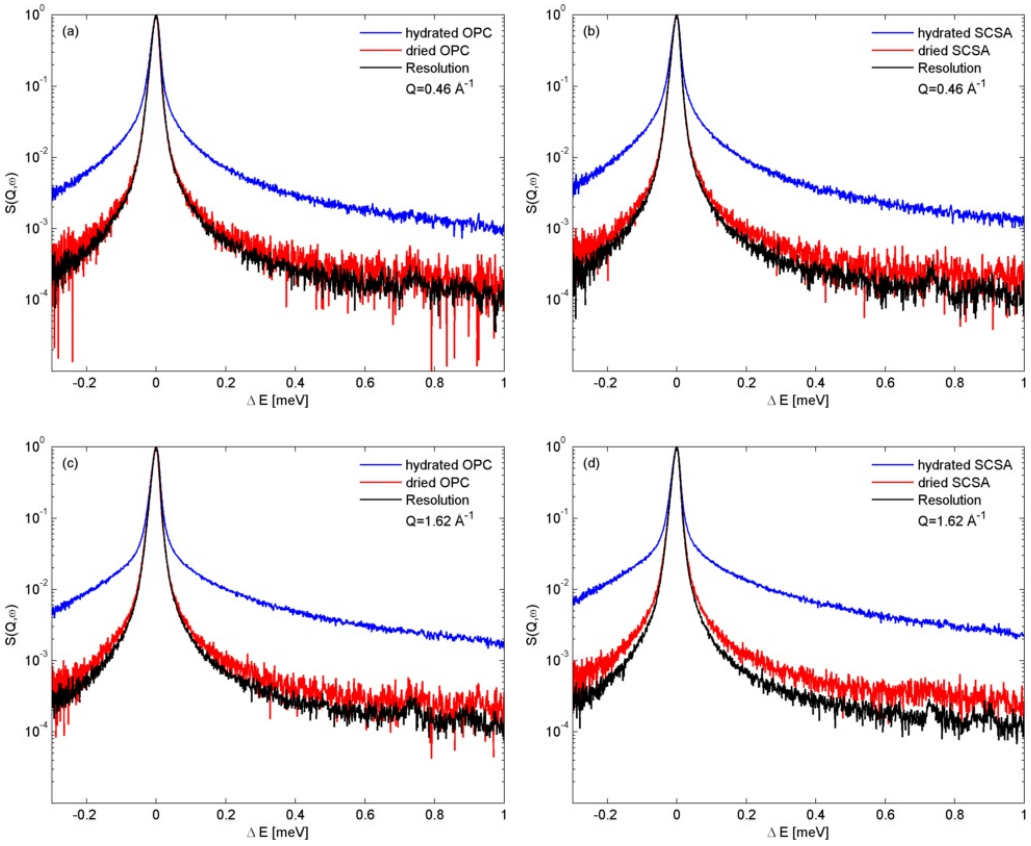

Figure 4.2: *Examples of typical QENS spectra obtained on dried cement pastes (red), hydrated cement pastes (blue) and on resolution function, obtained from hydrated cement pastes at* 10 *K (black). ISIS spectra were recorded with* $\Delta E = 17.5\ \mu eV$ *on 28 days old samples of OPC and M700 preppared with water to cement ratio of* 0.45*. Spectra are normalized to unity.*

samples, red indicates dried samples and black is a resolution measurement taken from a hydrated sample cooled to 5 K. The spectra are normalized to unity for comparison. For all spectra a QE broadening of the elastic signal is clearly seen in the hydrated samples. In the dried samples a small broadening is also visible, and it is clearer in the high-Q spectra (4.2(c)) and 4.2(d)) than in the low-Q spectra (4.2(a)) and 4.2(b)). As mentioned above, while the broadening in the hydrated samples is from hydrogen in confined as well as *bound water*, the broadening in the dried samples is only from hydrogen in *bound water*. This is in full agreement with the EFW results.

As the signal from structural hydrogen was removed by subtracting the dried spectra from the hydrated spectra, the resulting spectra are expected to contain only signal from the *confined water*. Since the *confined water* consists of both *glass-like* and *bulk-like* water, and both groups are seen in the EFW results, it is possible that these can be separated in the QENS analysis. First however, this was assumed not be the case and the QENS spectra were analyzed using the single Lorentzian model (Eq. (2.33)) derived in Section 2.5:

$$S\left(Q,\omega\right) = e^{-\frac{1}{3}\left\langle u(T)^2\right\rangle Q^2}\left[\left(A_0(Q)\delta(\omega) + (1-A_0)(Q)L\left(\Gamma,\omega\right)\right) \otimes R(Q,\omega)\right]. \tag{4.1}$$

Under this model we assume that the *bound water* will contribute to the elastic part of the QENS spectrum, while the *confined water* will give rise to a QE broadening described by a Lorentzian.

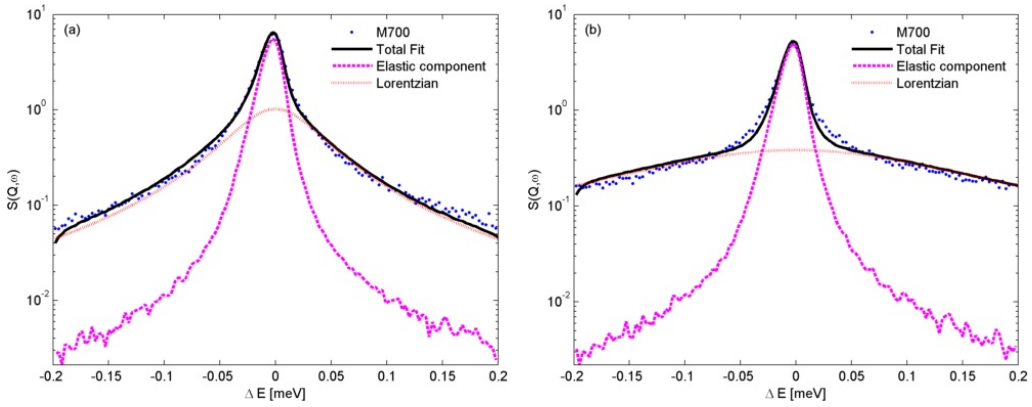

Figure 4.3: *Experimental QE spectra for M700 at* 300 K *at selected Q-values,* $Q = 0.463$ $\mathring{A}^{-1}$ *(a) and* $Q = 1.62$ $\mathring{A}^{-1}$ *(b);* $\Delta E = 17.5$ μeV*. From the figure we observe that a single Lorentzian model is insufficient to describe the data as the elastic signal has a QE broadening that is unaccounted for.*

This single Lorentzian model was used to fit the spectra in each of the 18 groups for OPC and M700. Figure 4.3 shows the result for the M700 $Q = 0.463$ Å^{-1} and $Q = 1.62$ Å^{-1} spectra fit obtained using the program DAVE [72]. The total fit contains an elastic and a QE component. For the low Q spectra the fits were reasonable, but as Q increased the necessity to account for the broadening became increasingly apparent. This was the case for both the OPC and the M700 samples.

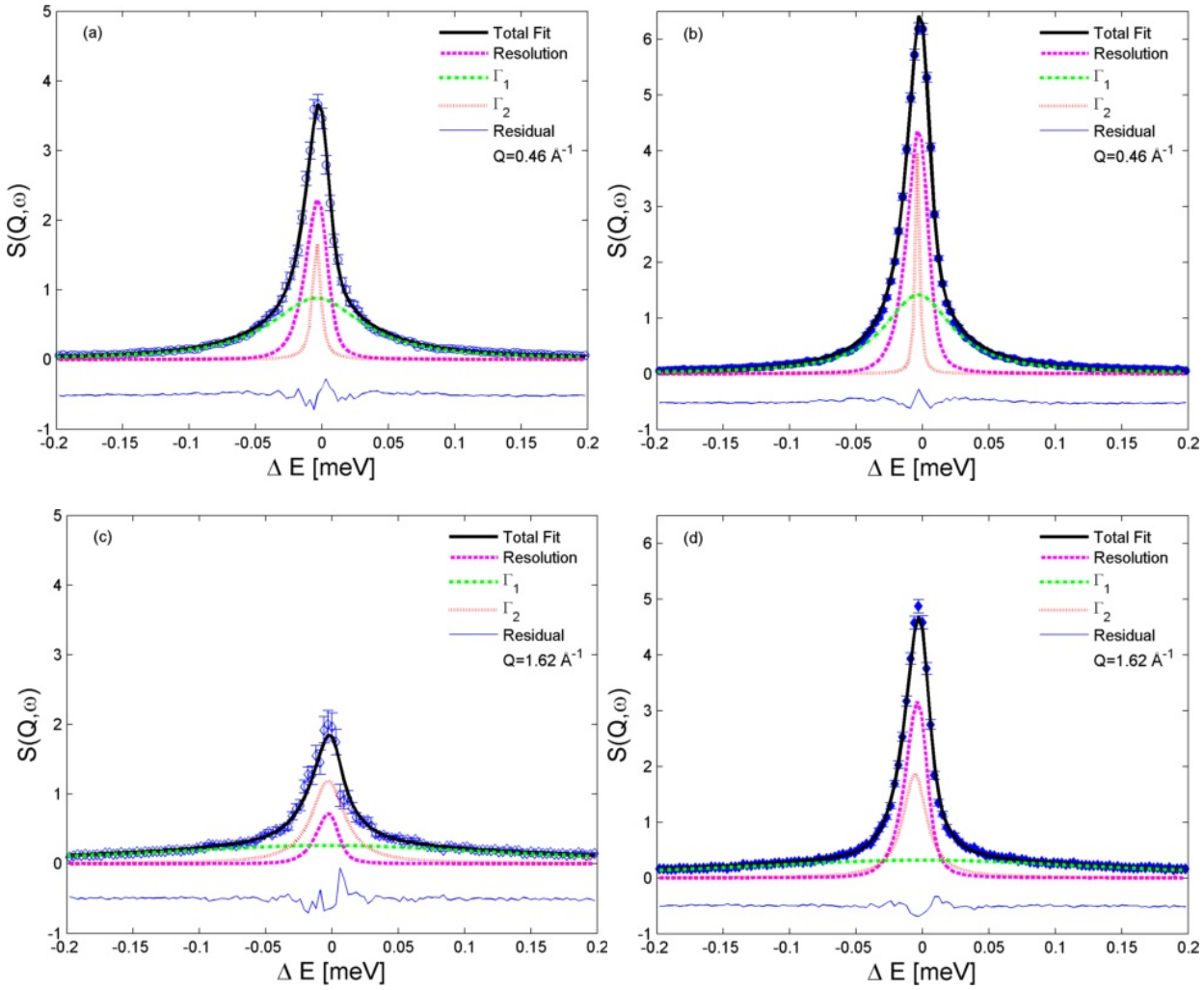

Figure 4.4: *Experimental QE spectra for OPC and M700 at* 300 K *at selected Q-values;* $\Delta E = 17.5\ \mu eV$. *OPC spectra are shown in (a) and (c). M700 spectra are shown in (b) and (d).*

Therefore, we confirmed that a second Lorentzian component is needed to fit the data properly. The requirement of two Lorentzians also confirms our assumption for the presence of two separate water populations within the cement pastes, with different water dynamics. Based on Eq. (2.35), the model was expanded to include a second Lorentzian:

$$S\left(Q,\omega\right) = e^{-\frac{1}{3}\left\langle u(T)^2\right\rangle Q^2}\left[\left(A_0(Q)\delta(\omega) + \sum_{i=1}^{2} A_i(Q)L_i\left(\Gamma_i,\omega\right)\right) \otimes R(Q,\omega)\right]. \tag{4.2}$$

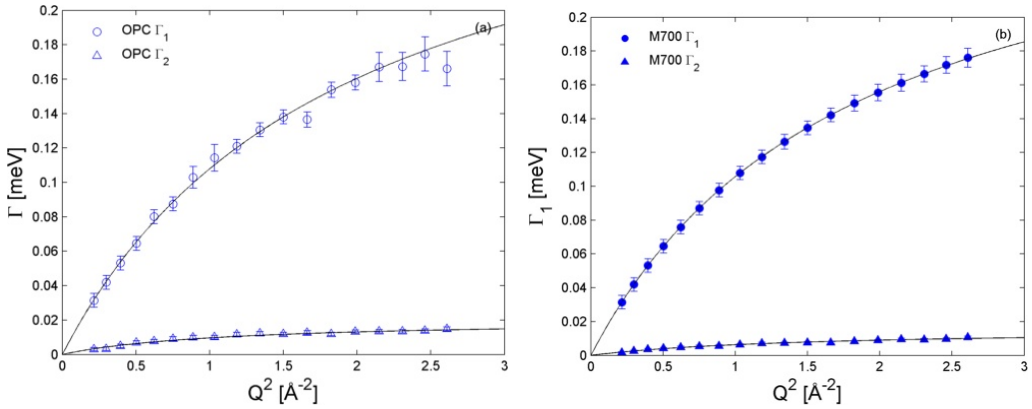

Figure 4.5: *OPC and M700 Lorentzian HWHM fitted to the Singi-Sjölander model.*

Figure 4.4 shows the fit results from DAVE with the 2-Lorentzian model for the lowest and highest Q-spectra for OPC (4.4(a) and 4.4(c)) and M700 (4.4(b) and 4.4(d)). The residual from the fits are shown in addition to the total fits with their elastic and Lorentzian components. All 36 fits had a reduced Chi-square close to 1 and the 2-Lorentzian model was accepted.

The Q dependencies of the Lorentzian widths for both samples are shown in Figure 4.5. They have been fitted to the Singwi-Sjölander model, which is described in Section 2.4.3. The actual function used to obtain the values in Table 4.1 is given in appendix C. The obtained parameter values are given in Table 4.1.

Each Lorentzian can be associated with a distinct water population within the cement pastes, an overview of which is given in Section 3.2. For both OPC and M700, the broad Γ_1 Lorentzians have diffusion coefficients (D_t) similar to *bulk water*. Therefore these Lorentzians can be associated with the *bulk-like* water populations found in capillary pores. The slightly increased relaxation time (τ_0) indicates that this *bulk-like* water does not show tetragonal symmetry [66].

In both samples the narrow Γ_2 Lorentzians have a significantly lowered diffusion coefficient and a greatly increased relaxation time compared to *bulk water*. Since confining water shifts the mobility to longer relaxation times and slower diffusion rates, these Lorentzians are associated with the *glass-like* water restricted in the gel pores.

Table 4.1: *Parameters characterizing the diffusional motions found in 28 days old OPC and M700 cement pastes with a water to cement ratio of* 0.45 *measured at* 300 K *and* ΔE *(FWHM)* = 17.5 μeV. *Values for bulk water are given as reference.*

	τ_0 (ps)	D_t (10^{-9} m^2/ s)
Bulk Water	1.57 ± 0.12	2.49 ± 0.07
OPC Γ_1	2.1 ± 0.3	2.5 ± 0.4
OPC Γ_2	32.3 ± 0.5	0.28 ± 0.04
M700 Γ_1	2.21 ± 0.02	2.49 ± 0.02
M700 Γ_2	41.9 ± 0.3	0.16 ± 0.01

4.1.3 Elastic Incoherent Structure Factor

As explained in Sections 2.3.3 and 2.5, determination of the EISF is necessary to obtain information on the geometry in which the observed motions take place. Eq.(2.34) defines the EISF as the fraction of total scattering intensity contained in the purely elastic peak; or equivalently, how much of the total signal is elastic.

Since the total scattering intensity, in our case, is a sum of the elastic intensity and two separate QE intensities, the EISF describes the geometry of both diffusive motions collectively. In order to separate the geometry of the two motions and investigate the behavior of the *glass-like* water population, an "effective" EISF is found. This is done by taking the total scattering intensity to be the sum of the elastic intensity and the QE intensity. In this way an "effective" EISF is obtained. Figure 4.6 shows the effective EISF for slower moving *glass-like* water populations found in the OPC and M700 cement pastes.

For both samples, in the high Q region the EISF decreases with increasing Q, without approaching zero, indicating that a fraction of the water molecules are immobile in the examined time-space window. In the M700 the EISF also shows an increase with Q after reaching a local minimum around $Q = 1$ Å^{-1}. This is yet another indication that the *bulk-like* water is somehow being restricted in its rotational motion. Moreover, in the low Q limit, the EISF approaches unity for both samples. This indicates localized dynamics that do not allow the water to diffuse over long distances.

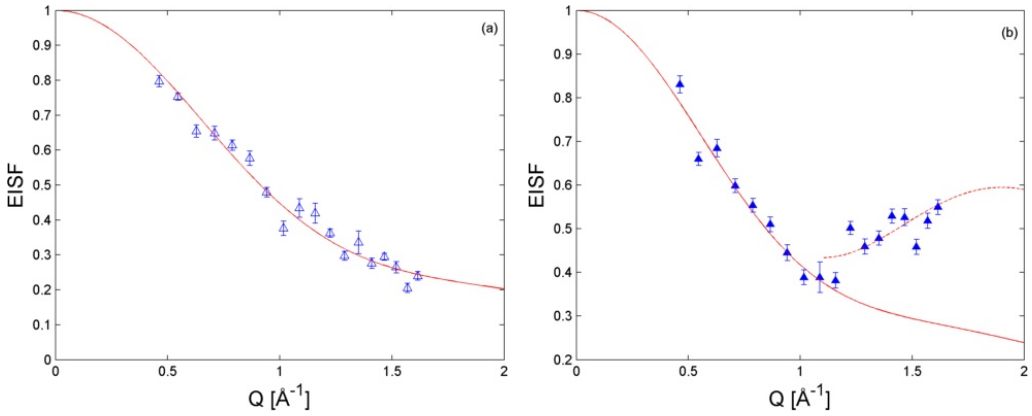

Figure 4.6: *The EISF vs. Q for OPC (a) and M700 (b) obtained from QENS spectra fits in DAVE. The effective EISF is plotted with triangles for the narrow Lorentzian component and circles for the broad Lorentzian component. The solid lines are obtained using the models described in the text.*

In order to analyze the geometry of the motion, we consider the simplest model for the translational motion of a water molecule in a confined space: diffusion of a point particle inside a sphere of radius a. The EISF of such a motion is described by the Volino-Dianoux model [48]:

$$EISF = \left[\frac{3j_1(Qa)}{Qa}\right]^2, \tag{4.3}$$

where j_1 is the first order spherical Bessel function and a is the radius of the sphere. This model was modified to account for the immobile fraction of protons, p, present in the sample and the Debye-Waller factor was included to account for the vibrational motions:

$$EISF = exp(-0.125 \cdot Q^2) \cdot \left(p + (1-p)\left[\frac{3j_1(Qa)}{Qa}\right]^2\right), \tag{4.4}$$

$\langle u^2 \rangle = 0.125$ Å^2 being the mean-square vibrational amplitude of hydrogen atoms in water at room temperature [49].

The fit result is shown in Figure 4.6(a) and the obtained parameters are:

$$p = 0.33 \pm 0.04 \text{ and } a = 2.5 \pm 0.2 \text{ Å}.$$

This indicates that the translational motion of the *glass-like* water found in the gel pores of OPC is confined to a 2.5 Å radius sphere. Approximately 33% of the *glass-like* water confined in the gel pores is seen to be immobile.

It is believed that a significant amount of the gel water will be confined in interlayers similar to those found in clays [76]. It is probable that the observed immobile fraction of *glass-like* water is confined in this interlayer space.

For the M700 sample shown in Figure 4.6(b) this simple model is insufficient as indicated by the full line.

The effective EISF was then divided into two parts that were fitted with separate models. In the region with $Q < 1$ Å^{-1} the effective EISF was fitted to the same model as in the OPC case. The resulting fit parameters show that $27 \pm 5\%$ of the protons are immobile and the diffusive process takes place within a 2.6 ± 0.1 Å radius sphere, while the region with $Q > 1$ Å^{-1} the effective EISF was fitted to a 2-site jump model:

$$EISF = p + (1-p)\frac{1}{2}\left[1 + \frac{sin(Qd)}{Qd}\right], \tag{4.5}$$

where p is the fraction of immobile hydrogen and d is the distance between jump sites. This model describes the hydrogen as jumping between two sites a distance d apart. The parameter values obtained from the fits are:

$$p = 0.07 \pm 0.04 \text{ and } d = 4.5 \pm 0.4 \text{ Å}.$$

From these values we see that about 7% of the hydrogen is immobile and the remaining hydrogen is confined to jumping between sites 4.5 Å apart.

4.2 Discussion

As explained in Section 3.2 the cement pastes analyzed here contain 3 types of protons categorized in two water populations; *bound water* containing structural hydrogen and *confined water* containing hydrogen in *glass-like* and *bulk-like* water. By drying the samples at 105° C the *confined water* was removed and EFW scans were performed on both hydrated and dried samples. In the dried sample the presence of hydrogen in OH groups bound to the surface of the pore structure was detected. The EFW scans on the hydrated samples clearly show the two distinct *confined water* populations, *glass-like* water confined in the gel pores and a *bulk-like* water located in the larger capillary pores.

By analyzing the QENS spectra of the two hydrated samples, the two *confined water* populations were clearly identified in each sample. The *bulk-like* water population shows diffusive properties similar to *bulk water*, but with a slightly increased relaxation time. This indicates that while these populations diffuse almost freely, they are restricted in their motions. The *glass-like* water populations in the gel pores have diffusive properties that clearly show the water to be confined. A comparison of the values found for OPC and M700 show that the *glass-like* water in the M700 sample diffuses slower and with a longer relaxation time than in the OPC case. This indicates that water motion in the M700 sample is more restricted by the added pozzolans. An analysis of the effective EISFs show that the translational motions are confined to spheres of roughly the same size in the two samples.

However, and more importantly, the effective EISF analysis of the M700 sample shows that a rotational restriction is observed. This can be related to water molecules reacting with the pozzalans that fills the pores. Thus, the hydrogen atoms become bound to the pozzolan structure and are no longer able to diffuse freely, but instead jump between separated sites. It should be noted that the distance, d, found corresponds well to the distance between two neighboring H sites in H_2O.

4.3 Conclusion and Outlook

Using neutron spectroscopy, we have studied a cement (M700) blended with pozzolanic ash from sugarcane residuals originating from agro-industrial waste and compared it to ordinary Portland cement (OPC). We have shown that the hydration process in M700 is slower after 28 days than in OPC. Despite this, the water in the M700 cement is more restricted. The added pozzolans in the M700 cement fill the pores and react with the *confined water*, binding it to the developing cement structure and creating a distinct hydrogen-bond network on the nano-scale. As a result, motions of the unreacted *confined water* become even more hindered slowing the diffusion of the water through the pores when compared to OPC.

In a time when the world's increasing need for expanding infrastructure is countered by financial crisis and climate change issues, the need for efficient, sustainable, durable and cleaner building materials has never been greater. Maintenance-free concrete made from blended cements have ad-

vantages over ordinary cement, they are cheaper, generate less CO_2 and are more durable. The improved performance of blended cements is linked to their ability to resist water penetration. Using QENS we have shown that the development of a distinct hydrogen-bond network is the key to this water resistance and the enhanced performance of the greener cement. Hopefully this understanding will lead to increased applications of greener cements.

Chapter 5

The Setting Process in Glass Ionomer Cements

This chapter presents the results of the dental cement hydration experiments described in Section 3.3. The evolution of the incoherent elastic signal for the AQUA and POLY samples, measured using IRIS and IN10, are presented in the form of an immobile hydrogen index (IHI) as a function of maturation time. After the results are discussed a conclusion of the experiment is presented together with an outlook on future experiments.

As described in Section 3.3.3, the IHI is defined as:

$$\text{IHI} = \frac{\text{elastic intensity}}{\text{total intensity}}. \tag{5.1}$$

In studies of the hydration process in construction cement, the IHI is referred to as the *bound water index* (BWI) and is used together with the *free water index* (FWI), FWI = 1−BWI, to determine the degree of reaction in the setting process [79],[80]. Considering that the hydration process in construction cement is much slower than in the GIC, which set within minutes, the Avrami model [81]–[83], used to analyze the pore structure formation through the FWI and the BWI indexes, is not applicable in our study. However, the long time evolution of the hydrogen bond formation can be analyzed using a similar exponential growth approach.

The GIC setting process begins immediately after the mixing of the aqueous liquid and the cement powder and undergoes several stages [84]. As the cement matures, more and more hydrogen will become chemically bound within the sample. Therefore, by analyzing this maturation process using an exponential growth approach it is possible to distinguish different phases of the setting process, and describe each phase with associated relaxation times. This comparison will allow a quantitative analysis of the differences between the phases.

5.1 Results

Figures 5.1 and 5.2 show the IHI of the AQUA and POLY cements as a function of time for the IRIS and IN10 experiments. The AQUA cement is shown in blue and the POLY cement is in red. Exponential growth fits are represented by the black lines. The first model used was mono-exponential growth:

$$\mathrm{IHI} = M_0 + M_1 \cdot exp\left(-t \cdot T_1\right), \tag{5.2}$$

where M_0 is the asymptotically approached IHI, M_1 is the initial IHI and T_1 is an inverse relaxation time. This model was proven to be insufficient, and consequently a second exponential component was introduced:

$$\mathrm{IHI} = M_0 + M_1 \cdot exp\left(-t \cdot T_1\right) + M_2 \cdot exp\left(-t \cdot T_2\right). \tag{5.3}$$

The obtained fit parameters are given in Table 5.1. Two distinct parts of the setting reaction are discernible in the IHI evolution in both experiments and their separation is indicated by a vertical dotted line at 100 min. Each of the two parts in the setting reaction requires their own exponential model, hence the need for a double exponential to describe the data properly. The inverse relaxation times in each exponential component describes the setting processes for these two distinct parts of the reaction. The initial part from $30-100$ minutes is described by T_1, while the second part from 100 minutes to 24 hours is described by T_2.

In conclusion, our results show that the hydration process in the two samples follows a very similar behavior, and that after 100 minutes, the setting process is seen to drastically change as the inverse relaxation times T_2 are more than a factor of 10 greater than the T_1 relaxation times.

In the IN10 experiment, as seen in Figure 5.2, the IHI is roughly the same for the two cements at the time when the measurements began. The IHI increases faster in the AQUA cement over time compared to the POLY cement and at 24 hours of hydration the IHI of the AQUA sample is visibly greater than that of the POLY sample. After 4 days (5760 minutes) of setting time passed, the IHI in the POLY sample is almost as high as that of the AQUA sample. This shows that the two cements reach the same degree of reaction after 4 days with different hydration processes. This difference is also reflected in the greater values of T_1 and T_2 found for the AQUA cement compared to the values found for the POLY cement. Just

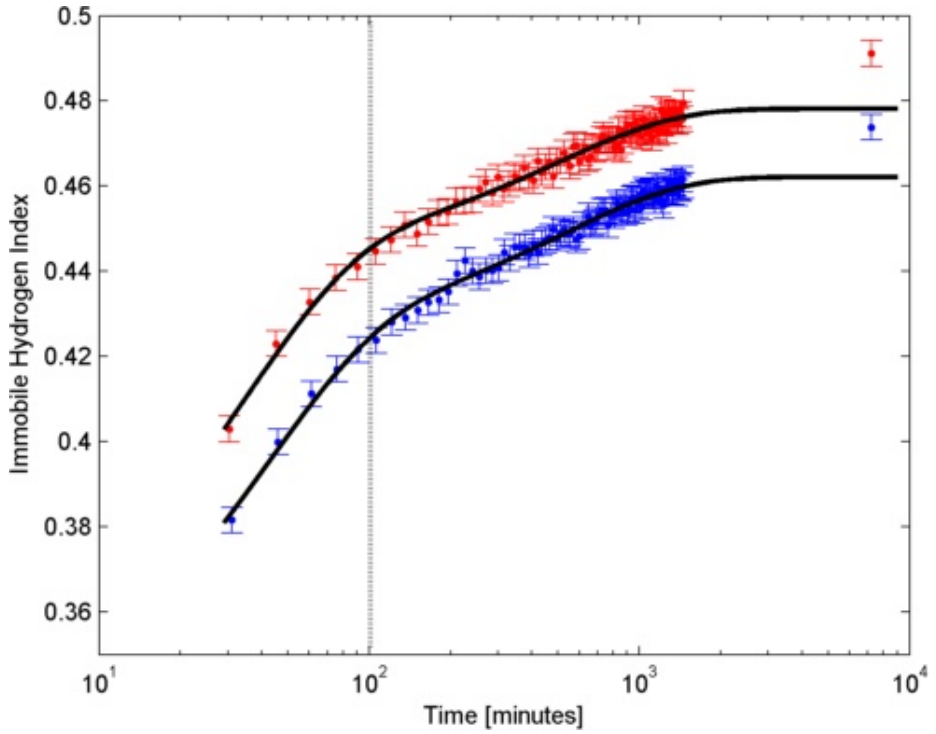

Figure 5.1: *The time evolution of the immobile hydrogen index (IHI) for the IRIS experiment on the ps time-scale. The AQUA sample is in blue and the POLY sample is in red. The measured IHI is fitted to an exponential growth model (black line) as described in the main text. The vertical dotted line indicates the threshold between two distinct parts of the setting reaction.*

like the IRIS experiment, a drastic change in the setting process is also observed at around 100 minutes, as once again the relaxation times T_2 are more than a factor of 10 greater than the T_1 relaxation times.

Table 5.1: *Parameters obtained from the IHI fits shown in Figures 5.1 and 5.2. M_0, M_1 and M_2 are dimensionless, while T_1 and T_2 are in units of inverse minutes, min^{-1}.*

	IRIS		IN10	
	AQUA	POLY	AQUA	POLY
M_0	0.462 ± 0.001	0.478 ± 0.001	0.619 ± 0.001	0.578 ± 0.002
M_1	-0.036 ± 0.001	-0.034 ± 0.001	-0.108 ± 0.002	-0.086 ± 0.002
T_1	0.0019 ± 0.0002	0.0020 ± 0.0002	0.0022 ± 0.0001	0.0019 ± 0.0001
M_2	-0.097 ± 0.005	-0.103 ± 0.009	-0.253 ± 0.015	-0.19 ± 0.01
T_2	0.025 ± 0.002	0.030 ± 0.003	0.034 ± 0.002	0.028 ± 0.002

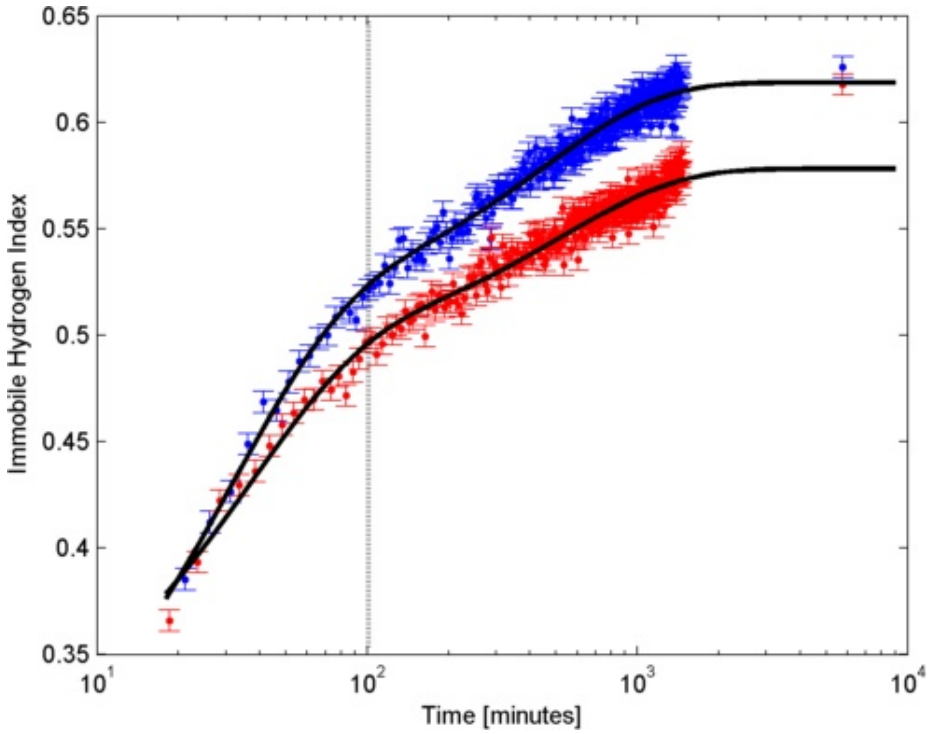

Figure 5.2: *The time evolution of the immobile hydrogen index (IHI) for the IN10 experiment on the ns time-scale. The AQUA sample is in blue and the POLY sample is in red. The measured IHI is fitted to an exponential growth model (black line) as described in the main text. The vertical dotted line indicates the threshold between two distinct parts of the setting reaction.*

5.2 Discussion

In both experiments, the setting process is seen to drastically change after 100 minutes, as indicated by the vertical line in Figures 5.1 and 5.2. The inverse relaxation times observed on both time-scales for both samples, increase by more than a factor 10 after the first 100 minutes of setting time. In order to understand the reason for this, an account of the setting process is needed.

The GIC setting process illustrated in Figure 5.3 begins immediately after the mixing of the aqueous liquid and the cement powder and undergoes several stages [84].

(i) In the initial stage the glass particles become dispersed in the liquid water and polyacid solution.

(ii) In the second stage the polyacid reacts with the glass powder, releasing Ca^{2+} and Al^{3+} ions. The outer surface of the glass particles becomes depleted of metal ions and degrades into a silica gel. The metal ions migrate into the liquid where they remain in a soluble form.

(iii) The third stage sees the formation of a salt hydrogel as the soluble metal ions bind to the polyacid forming metal polyacrylates. The pH also increases during this stage, reflecting the conversion of polyacid to polyacrylates.

(iv) In the final stage all metal ions are in an insoluble form.

The acid attack on the glass is not uniform, but occurs preferentially on calcium rich sites [85]. As a result the calcium polyacrylate is formed before aluminum polyacrylate, and is responsible for the initial setting of the cement.

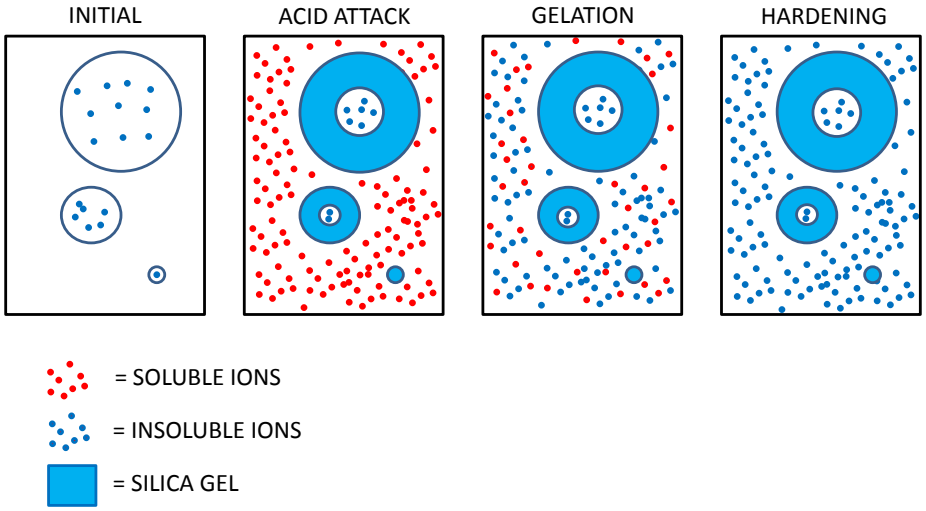

Figure 5.3: *The setting process of the GIC. In the initial state un-attacked glass particles are dispersed in the liquid polyacid. The blue dots represent metal ions bound in the glass. The acid attacks the glass reducing the outer layer to a silica gel. The released metal ions migrate to the liquid and remain in soluble form (red dots). When a sufficient number of metal ions have accumulated the gelation process begins and metal ions begin to become bound again. In the fully hardened cement the metal ions are no longer in soluble form. Figure is adapted from [84].*

Studies of the time dependence of soluble ions in the cement have shown that the calcium ions are almost fully combined after 100 minutes and within three hours this process is completed, whereas aluminum ions continue to react for at least 48 hours [86]. A study of the surface pH in different GIC revealed that it stabilizes after 100 minutes [84]. Therefore, the drastic change in the setting process observed at around 100 minutes, can be explained by the transition from the initial setting dominated by the fast formation of calcium polyacrylate into the subsequent setting process dominated by the slower forming aluminum polyacrylate.

Additionally, it is known that as the cement ages and the degree of hydration increases, an increase in compressive strength and elastic modulus is observed [85]. Therefore, the higher IHI observed with IRIS for the POLY cement can be directly related to the known greater compressive strength of the POLY cement compared to the AQUA. Finally the differences we see in the IN10 data can be explained by the faster initial setting of the POLY cement compared to the AQUA cement. In this initial setting, the formed cement matrix is dominated by calcium polyacrylate, increasing the density of cross-links and thus hindering the movement of aluminum ions towards the polyacids to which they bind. So, while the calcium polyacrylate forms quicker in the POLY cement, creating a stronger structure faster, this slows down the formation rate of the aluminum polyacrylates. The higher relative water content and the slower formation of calcium polyacrylate in the AQUA cement, makes it easier for the aluminum ions to move towards the polyacids in the AQUA cement. This enables a faster formation of aluminum polyacrylate in the AQUA sample than in the POLY sample and is the reason for the comparatively higher IHI throughout the first 24 hours of measurement.

5.3 Conclusion

Two phases of the setting process of the AQUA and POLY cements are clearly distinguishable. The first phase, which ends after approximately 100 minutes of setting time, is dominated by the formation of calcium polyacrylate. This is followed by the second phase in which the formation of aluminum polyacrylate dominates. These two phases are described by inverse relaxation times that differ by more than a factor of 10.

A couple of issues remain unresolved necessitating future studies. The hydration process is known to continue for several days, therefore measurements should be done on cements pastes older than 5 days, to determine when the change in the IHI reaches a plateau, as this will show how long it takes for the final structure to form.

It was not possible to begin measurements earlier than we did, for this reason, the initial setting process has not been studied. We can assume that immediately after the powder and liquid are brought together the IHI found in both instruments must be zero. Since the IHI found on IRIS is different for the two cements, the setting process is likely to follow different paths in the first 30 minutes. One possible way to study this early setting process is to somehow delay it by mixing the samples at lower temperature. Another possibility is to devise a sample holder which allows for the mixing of the liquid and powder components within the cryostat with the neutron beam on. This will also require the experiment to be done on an instrument with a good signal-to-noise ratio, in order to acquire data points in short time intervals, preferably faster than the 5 minute intervals in the IN10 experiment.

The final point I would like to make is that in this study the quasi-elastic broadening has not been analyzed, in a manner similar to that done in the construction cement experiment. An analysis and comparison of the QENS spectra of the two cements, in the periods before and after the change observed at 100 minutes, will shed further light on the differences between the calcium polyacrylate and the aluminum polyacrylate dominated setting phases.

Chapter 6

Concluding Remarks

In this work I have applied quasi-elastic neutron scattering on two systems, construction cement paste and dental restorative cement.

In the study of construction cement paste, I have shown how the inclusion of pozzolanic ashes changes the proton mobility in 28 days old matured pastes, by creating a distinct hydrogen bond network on the nano-scale. This finding helps to understand the enhanced performance of blended cements and will hopefully lead to increased applications.

The setting process in glass ionomer cements (GIC) has many aspects similar to that of construction cement; a powder and a liquid are brought together causing a reaction in which a solid structure is formed by hydrogen bonding. For this reason, we applied a similar approach to that already used in the study of construction cement hydration to the glass ionomer cements, namely the observation of the change on time of the incoherent elastic line intensity. This proved to be very successful, and key aspects in the setting processes of the two studied dental cements were identified in this work. For instance, the initial setting process dominated by the formation of calcium polyacrylate was shown to be clearly separated from the later setting process dominated by the formation of aluminum polyacrylate. Also by using two different instruments, covering different time domains, the changes in the liquid mobility were separated from those of the polyacid component. These results will undoubtedly lead to future studies of dental cement setting processes using neutrons.

Appendix A

The Double Differential Cross Section

In this Appendix Eq. (2.19) is derived from Eq. (2.18). The derivation is a combination of those given by Hempelmann [34] and Lovesey [21]. When an experiment is conducted, the measured quantity is the intensity of the scattered neutrons. When an energy exchange between neutron and sample takes place this intensity is given by:

$$dI = N\phi(\epsilon_i)\Delta\epsilon_i \frac{d^2\sigma}{d\Omega d\epsilon_f}\Delta\Omega\Delta\epsilon_f, \tag{A.1}$$

where N is the number of elements in the scattering volume, $\phi(\epsilon_i)$ is the neutron flux, $\Delta\epsilon_i$ is the incident neutron bandwidth, $\Delta\Omega$ is the collection solid angle and$\Delta\epsilon_f$ is the scattered neutron energy window. All these terms are fixed during the experiment as a result of instrument design and other factors such as the neutron source properties. The last term is the double differential cross section, this the part of the intensity that varies in the experiment. For unpolarized neutrons it can be expressed as:

$$\frac{\partial^2\sigma}{\partial\Omega\partial E_f} = \frac{k_f}{k_i}\sum_{i,f} P_i \left(\frac{m_n}{2\pi\hbar^2}\right) |\langle i|\,\mathbf{V}\,|f\rangle|^2\,\delta\left(E_f - E_i - \hbar\omega\right), \tag{A.2}$$

where i and f are the initial and final states respectively and $\mathbf{V}$ is the interaction potential between neutron and the nuclei, which is given by:

$$\mathbf{V}(\mathbf{r}) = \frac{2\pi\hbar^2}{m_n}\sum_j b_j\delta(\mathbf{r} - \mathbf{R}_j). \tag{A.3}$$

We now use this potential to expand the matrix element in the inelastic cross section:

$$\begin{aligned} |\langle i|\,\mathbf{V}\,|f\rangle|^2 &= |\langle \lambda_i\psi_i|\,\mathbf{V}\,|\lambda_f\psi_f\rangle|^2 && \text{(A.4)}\\ &= \frac{2\pi\hbar^2}{m_n}\left[\sum_j b_j \left\langle \lambda_i \left| \int \psi_i^*\delta(\mathbf{r}-\mathbf{R}_j)\psi_f d^3r \right| \lambda_f \right\rangle\right]^2 && \text{(A.5)}\\ &= \frac{2\pi\hbar^2}{m_n}\sum_{j,j'} b_j b_{j'} \left\langle \lambda_i \left| e^{-iQ\mathbf{R}_j} \right| \lambda_f \right\rangle \left\langle \lambda_f \left| e^{iQ\mathbf{R}_{j'}} \right| \lambda_i \right\rangle && \text{(A.6)} \end{aligned}$$

We can get rid of the delta-function by Fourier transforming it:

$$\begin{aligned} \delta\left(E_f - E_i - \hbar\omega\right) &= \frac{1}{2\pi}\int_{-\infty}^{\infty} e^{i(E_f-E_i)/\hbar-\omega)t}dt && \text{(A.7)}\\ &= \frac{1}{2\pi}\int_{-\infty}^{\infty} e^{i(E_f-E_i)/\hbar)t}e^{-i\omega t}dt && \text{(A.8)} \end{aligned}$$

We now use the completeness relation from quantum mechanics, $\sum_f \langle i|\,\mathbf{A}\,|f\rangle\langle f|\,\mathbf{B}\,|i\rangle = \langle i|\,\mathbf{AB}\,|i\rangle$, and introduce H instead of E_n by $e^{-iHt/\hbar}|i\rangle = e^{-iE_it/\hbar}|i\rangle$. As a result we can now write Eq. (A.2) as:

$$\frac{\partial^2\sigma}{\partial\Omega\partial E_f} = \frac{k_f}{k_i}\frac{1}{2\pi\hbar}\sum_i P_i \sum_{j,j'} b_j b_{j'} \int_{-\infty}^{\infty} \langle i|\, e^{-iQ\mathbf{R}_j} e^{iHt/\hbar} e^{iQ\mathbf{R}_{j'}} e^{-iHt/\hbar}\,|i\rangle\, e^{-i\omega t}dt. \tag{A.9}$$

We now address the time evolution of $\mathbf{R}$ by the operation:

$$e^{i\mathbf{QR}(t)} = e^{iHt/\hbar}e^{i\mathbf{QR}}e^{-iHt/\hbar}, \tag{A.10}$$

which leads to the following expression of the double differential cross section:

$$\frac{\partial^2\sigma}{\partial\Omega\partial E_f} = \frac{k_f}{k_i}\frac{1}{2\pi\hbar}\sum_{j,j'} b_j b_{j'} \int_{-\infty}^{\infty} \left\langle e^{-iQ\mathbf{R}_j(0)} e^{iQ\mathbf{R}_{j'}(t)} \right\rangle e^{-i\omega t}dt, \tag{A.11}$$

where the sum $\sum_i P_i$ is omitted from now on and $\langle\cdots\rangle$ means the thermal average over the expectation value. Since we are dealing with a sum over a very large number of sites j, j' the scattering lengths can be taken as an average. First we observe that:

$$\langle b_j b_{j'}\rangle = \begin{cases} \langle b^2\rangle & \text{if } j = j' \\ \langle b\rangle^2 & \text{if } j \neq j' \end{cases} \tag{A.12}$$

Using this we can separate the sums in Eq. (A.11) into a coherent and incoherent part, by the definitions in Eqs.(2.14) and (2.16):

$$\langle b_j b_{j'} \rangle = \langle b \rangle^2 + \delta_{j,j'} \left(\langle b^2 \rangle - \langle b \rangle^2 \right) \quad (A.13)$$

$$\langle b_j b_{j'} \rangle = b_{coh}^2 + \delta_{j,j'} b_{inc}^2 \quad (A.14)$$

This gives a double differential cross section with distinct coherent and incoherent contributions:

$$\frac{\partial^2 \sigma}{\partial \Omega \partial E_f} = \frac{k_f}{k_i} \frac{1}{2\pi\hbar} \Bigg[\langle b \rangle^2 \int_{-\infty}^{\infty} \sum_{j,j'} \left\langle e^{-iQ\mathbf{R}_j(0)} e^{iQ\mathbf{R}_{j'}(t)} \right\rangle e^{-i\omega t} dt + \\ + \left(\langle b \rangle - \langle b \rangle^2 \right) \int_{-\infty}^{\infty} \sum_{j} \left\langle e^{-iQ\mathbf{R}_j(0)} e^{iQ\mathbf{R}_j(t)} \right\rangle e^{-i\omega t} dt \Bigg] \quad (A.15)$$

We now introduce the coherent and incoherent intermediate scattering functions:

$$\mathrm{I}_{coh}(\mathbf{Q}, t) = \sum_{j,j'} \left\langle e^{-iQ\mathbf{R}_j(0)} e^{iQ\mathbf{R}_{j'}(t)} \right\rangle, \quad (A.16)$$

which includes contributions from all terms and the function $I_{inc}(\mathbf{Q}, t)$ containing the contributions from the self terms,

$$\mathrm{I}_{inc}(\mathbf{Q}, t) = \sum_{j} \left\langle e^{-iQ\mathbf{R}_j(0)} e^{iQ\mathbf{R}_j(t)} \right\rangle. \quad (A.17)$$

If we take the Fourier transforms with respect to time of the intermediate scattering functions we obtain the *coherent and incoherent dynamical structure factors*, more commonly known as the *scattering functions*.

$$\mathrm{S}_{coh}(\mathbf{Q}, \omega) = \frac{1}{2\pi\hbar} \int_{-\infty}^{\infty} \sum_{j,j'} \left\langle e^{-iQ\mathbf{R}_j(0)} e^{iQ\mathbf{R}_{j'}(t)} \right\rangle e^{-i\omega t} dt \quad (A.18)$$

$$\mathrm{S}_{inc}(\mathbf{Q}, \omega) = \frac{1}{2\pi\hbar} \int_{-\infty}^{\infty} \sum_{j} \left\langle e^{-iQ\mathbf{R}_j(0)} e^{iQ\mathbf{R}_j(t)} \right\rangle e^{-i\omega t} dt \quad (A.19)$$

All this allows us to express the double differential cross section in a much simplified way:

$$\boxed{\frac{\partial^2 \sigma}{\partial \Omega \partial E_f} = \frac{\sigma_{coh}}{4\pi\hbar} \frac{\mathrm{k}_f}{\mathrm{k}_i} \mathrm{S}_{coh}(Q, \omega) + \frac{\sigma_{inc}}{4\pi\hbar} \frac{\mathrm{k}_f}{\mathrm{k}_i} \mathrm{S}_{inc}(Q, \omega)} \quad (A.20)$$

Appendix B

Vibrational Motion and the Debye-Waller Factor

The purpose of this appendix is to derive Eq. (B.13), which gives the relation between the intensity of the elastic scattering function and the Debye-Waller factor. This relation describes how temperature dependent vibrational motions affect the elastic intensity as function of temperature. The derivation given is based on chapter 3.5 in Rolf Hempelmanns book [34]

An isolated harmonic oscillator is a reasonable model to describe a vibrating atom. We consider first the case where the system is in its ground state by lowering the temperature sufficiently, experimentally this is done by lowering the sample temperature to 5 K. It is well known from quantum mechanics [30] that for the harmonic oscillator the ground state and the first excited state wave functions are:

$$|0\rangle = \sqrt{\frac{\alpha}{\sqrt{\pi}}} e^{-\frac{1}{2}\alpha^2 x^2}, \tag{B.1}$$

$$|1\rangle = \sqrt{\frac{2\alpha^3}{\sqrt{\pi}}} x e^{-\frac{1}{2}\alpha^2 x^2}, \tag{B.2}$$

were $\alpha^2 = \frac{m\omega}{\hbar}$. The mean square displacement of the atom around its equilibrium position in the ground state is then:

$$\left\langle x^2 \right\rangle = \langle 0| \, x \, |0\rangle = \frac{\hbar}{2m\omega} = \frac{1}{2\alpha^2}. \tag{B.3}$$

Since what we measure in an experiment is an intensity:

$$dI = N\phi(\epsilon_i)\Delta\epsilon_i \frac{d^2\sigma}{d\Omega d\epsilon_f} \Delta\Omega \Delta\epsilon_f \tag{B.4}$$

we would like to evaluate the double differential cross section Eq. (2.19). From Hempelmann we know that this is much simplified in the case where the system is in the ground state:

$$\frac{d^2\sigma}{d\Omega d\epsilon_f} = \frac{\sigma}{4\pi\hbar}\frac{\mathrm{k}_f}{\mathrm{k}_i}\sum_{n=0}^{\infty}\mathrm{S}_{0\to n}(Q,\omega) \tag{B.5}$$

with the scattering function for the transition from $|0\rangle$ to $|n\rangle$ given by:

$$\mathrm{S}_{0\to n}(Q,\omega) = \left|\langle n|\, e^{iQx}\,|0\rangle\right|^2 \delta\left(\hbar\omega - n\hbar\omega_0\right), \tag{B.6}$$

where $n\hbar\omega_0$ is the energy difference between the ground state and the n'th state, see Figure(B.1). Since the system we are considering consists of in-

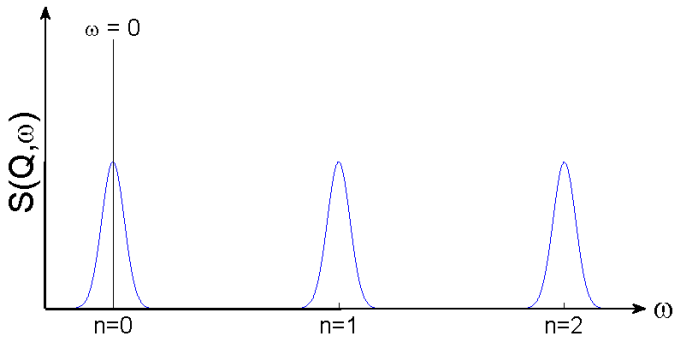

Figure B.1: *The δ-function in Eq. (B.6) ensures that a peak will only be seen when the energy transfered to or from the neutron by the sample equals the energy difference between the final and initial state. For $n = 0$ there is no energy difference and the signal is purely elastic located at 0. For $n \neq 0$ the peak becomes positioned at $n\hbar\omega$*

dependent oscillators vibrating without mutual interaction and phase relationship there are no distinct terms in the coherent scattering cross-section. The scattering cross-section in Eq. (B.5) is therefore the total scattering cross-section, as there is no distinction between coherent and incoherent scattering. Vibrational transitions from $|0\rangle$ to $|n\rangle$, $n = 1, 2, 3, ...$ give rise to inelastic scattering intensity. When the system is in its ground state we need to consider the transition from $|0\rangle$ to $|0\rangle$:

$$\langle 0|\, e^{iQx}\,|0\rangle = \int_{-\infty}^{\infty}\Psi_0^* e^{iQx}\Psi_0 dx \tag{B.7}$$

$$= e^{-Q^2/4\alpha^2} \tag{B.8}$$

By using the mean square displacement found in Eq. (B.3) we obtain:

$$\langle 0|\, e^{iQx}\, |0\rangle = e^{-\frac{1}{2}Q^2\langle x^2\rangle} = e^{-W}. \tag{B.9}$$

Then by inserting this value in Eq. (B.6) we get:

$$\mathrm{S}_{0\to 0}(Q,\omega) = e^{-2W}\delta(\hbar\omega), \tag{B.10}$$

where e^{-2W} is the Debye-Waller factor. Since the vibrations of the individual hydrogen atoms are 3-dimensional in nature we expand to a 3-dimensional oscillator, and the Debye-Waller factor then becomes:

$$e^{-2W} = e^{-\frac{1}{3}\langle u^2\rangle Q^2}. \tag{B.11}$$

Eq. (B.10) can now be written as:

$$\mathrm{S}_{0\to 0}(Q,\omega) = e^{-\frac{1}{3}\langle u(T)^2\rangle Q^2}\delta(\hbar\omega). \tag{B.12}$$

This relation is shown in Figure B.2.

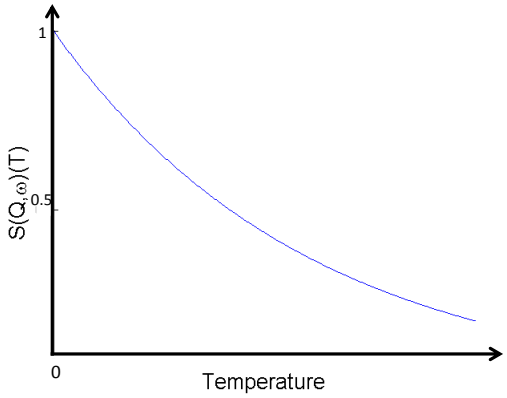

Figure B.2: *This figure shows the scattering function with $\omega = 0$ as a function of temperature. For a temperature of 0 K all scatterers are immobile, and contribute to the elastic signal. As the temperature increases the amount of immobile scatterers decreases. Subsequently the intensity of the elastic signal decreases. This decrease is given by the Debye-Waller factor.*

As the temperature of the system is increased the occupation of excited states becomes allowed and the mean atomic displacement from the equilibrium increases. As a result the Debye-Waller factor becomes temperature dependent. Additionally, since occupation of the excited states is

allowed at higher temperatures, the scattering functions $1 \rightarrow 1, 2 \rightarrow 2, ...$ also contribute to the elastic scattering, because $\omega = 0$ for these transitions. In principle due to the δ-function, only the scattering functions $0 \rightarrow 0, 1 \rightarrow 1, \cdots n \rightarrow n, ...$ contribute to the elastic scattering. However, due to several factors, like the mosaicity of the analyzer blades, the energy resolution of an instrument is not a δ-function. If the energy difference between two states n, m is smaller than the energy resolution of the instrument then the associated scattering function $S_{n \rightarrow m}$ will also contribute to the elastic signal. We consider $\omega \approx 0$ when it is sufficiently small as to lie within the instrument energy resolution. As a result the intensity of the elastic scattering function is given by the Debye-Waller factor:

$$\boxed{S_{elastic}(Q, \omega \approx 0)(T) = e^{-\frac{1}{3}\left\langle u(T)^2 \right\rangle Q^2}} \tag{B.13}$$

Appendix C

Units in the Singwi-Sjölander Model

In the Singwi-Sjölander model the Q-dependence of the Lorentzian half-widths, Γ, is given by:

$$\Gamma(Q) = \frac{\hbar \cdot D_t \cdot Q^2}{1 + \cdot D_t \cdot \tau_0 \cdot Q^2}, \tag{C.1}$$

were the Γ is in units of meV and the momentum transfer, Q, is in units of Å^{-1}. In order to have the diffusion coefficient, D_t, in units of 10^{-9} m^2 s^{-1} and the relaxation time τ_0 in units of ps, a conversion factor is needed in the numerator and the denominator as well as a proper choice of units for $\hbar$.

For $\hbar$ we choose units of meVs, $\hbar = 6.582 \cdot 10^{-13}$ meVs and since Q is in units of Å^{-1} we have:

$$Q^2 = \left(\text{Å}^{-1}\right)^2 = \left(10^{-10}\text{ m}\right)^{-2} = 10^{20}\text{ m}^{-2}. \tag{C.2}$$

Considering first the denominator, we notice that $D_t \cdot \tau_0 \cdot Q^2$ must be dimensionless and inserting the desired units for D_t and τ_0 we get:

$$\begin{aligned} D_t \cdot \tau_0 \cdot Q^2 &= (10^{-9}\text{ m}^2\text{ s}^{-1}) \cdot (10^{-12}\text{ s}) \cdot (10^{20}\text{ m}^{-2}) && \text{(C.3)} \\ &= 0.1, && \text{(C.4)} \end{aligned}$$

which is the required conversion factor.
For the numerator we get:

$$\begin{aligned} \hbar \cdot D_t \cdot Q^2 &= (6.582 \cdot 10^{-13}\text{ meVs}) \cdot (10^{-9}\text{ m}^2\text{ s}^{-1}) \cdot (10^{20}\text{ m}^{-2}) && \text{(C.5)} \\ &= 0.06582\text{ meV}, && \text{(C.6)} \end{aligned}$$

Which is the required conversion factor for a Lorentzian half-width in units of meV. As a result, the Singwi-Sjölander model in the desired units is:

$$\Gamma(Q) = \frac{0.06582 \cdot D_t \cdot Q^2}{1 + 0.1 \cdot D_t \cdot \tau_0 \cdot Q^2} \tag{C.7}$$

Bibliography

[1] J. Dotto, A. Abreu, D. D. Molin, and I. Müller, "Influence of silica fume addition on concretes physical properties and on corrosion behavior of reinforcement bars", *Cement and Concrete Composites*, volume 26, number 1, pages 31 –39, 2004, ISSN: 0958-9465. DOI: 10.1016/S0958-9465(02)00120-8 (cited on page iii).

[2] (Apr. 22, 2013). Voco webpage, [Online]. Available: http://www.voco.com/en/news/index.html (cited on page iv).

[3] C. Cardona, J. Quintero, and I. Paz, "Production of bioethanol from sugarcane bagasse: Status and perspectives", *Bioresource Technology*, volume 101, number 13, pages 4754 –4766, 2010, Special Issue on Lignocellulosic Bioethanol: Current Status and Perspectives, ISSN: 0960-8524. DOI: 10.1016/j.biortech.2009.10.097 (cited on page 1).

[4] A. Pandey, C. R. Soccol, P. Nigam, and V. T. Soccol, "Biotechnological potential of agro-industrial residues. I: sugarcane bagasse", *Bioresoure Technology*, volume 74, number 1, pages 69 –80, 2000, ISSN: 0960-8524. DOI: 10.1016/S0960-8524(99)00142-X (cited on page 1).

[5] W. A. Pippo, P. Garzone, and G. Cornacchia, "Agro-industry sugarcane residues disposal: The trends of their conversion into energy carriers in Cuba", *Waste Management*, volume 27, number 7, pages 869 –885, 2007, ISSN: 0956-053X. DOI: 10.1016/j.wasman.2006.05.001 (cited on page 1).

[6] M. Frías, E. Villar, and H. Savastano, "Brazilian sugar cane bagasse ashes from the cogeneration industry as active pozzolans for cement manufacture", *Cement and Concrete Composites*, volume 33, number 4, pages 490 –496, 2011, ISSN: 0958-9465. DOI: 10.1016/j.cemconcomp.2011.02.003 (cited on page 2).

[7] F. Martirena, B. Middendorf, R. L. Day, M. Gehrke, P. Roque, L. Martínez, and S. Betancourt, "Rudimentary, low tech incinerators as a means to produce reactive pozzolan out of sugar cane straw", *Cement and Concrete Research*, volume 36, number 6, pages 1056 –1061, 2006, ISSN: 0008-8846. DOI: 10.1016/j.cemconres.2006.03.016 (cited on page 2).

[8] *The cement sustainability initiative: Progress report*, World Business Council for Sustainable Development, 2002. [Online]. Available: http://csiprogress2012.org/ (cited on page 2).

[9] T. Powers and R. Helmuth, *Theory of Volume Changes in Hardened Portland Cement Paste During Freezing*, series Research department bulletin. Portland Cement Association, 1953 (cited on page 2).

[10] H. N. Bordallo and L. P. Aldridge, "Concrete and Cement Paste Studied by Quasi-Elastic Neutron Scattering", *Zeitschrift für Physikalische Chemie*, volume 224, number 1-2, pages 183 –200, 2010, ISSN: 0942-9352. DOI: doi:10.1524/zpch.2010.6098 (cited on pages 2, 3, 52).

[11] S. Mindess, J. Young, and D. Darwin, *Concrete*. Prentice Hall PTR, 2003, ISBN: 9780130646323. [Online]. Available: http://books.google.dk/books?id=38VoQgAACAAJ (cited on page 3).

[12] A. Neville, *Properties of concrete*. John Wiley & Sons, 1996, ISBN: 9780470235270. [Online]. Available: http://books.google.dk/books?id=mKEeAQAAIAAJ (cited on page 3).

[13] R. Bagramian, F. Garcia-Godoy, and A. Volpe, "The global increase in dental caries. A pending public health crisis.", *American journal of dentistry*, volume 21, number 1, pages 3–8, 2009, ISSN: 0894-8275. [Online]. Available: http://www.amjdent.com/Archive/2009/Bagramian%20-%20February%202009.pdf (cited on page 3).

[14] P. E. Petersen, D. Kandelman, S. Arpin, and H. Ogawa, "Global oral health of older people–call for public health action", *Community Dental Health*, volume 627, number 4, Supplement 2, pages 257–267, 2010, ISSN: 0265-539x. [Online]. Available: http://www.ncbi.nlm.nih.gov/pubmed/21313969 (cited on page 3).

[15] C. Whitters, R. Strang, D. Brown, R. Clarke, R. Curtis, P. Hatton, A. Ireland, C. Lloyd, J. McCabe, J. Nicholson, S. Scrimgeour, J. Setcos, M. Sherriff, R. van Noort, D. Watts, and D. Wood, "Dental materials: 1997 literature review", *Journal of Dentistry*, volume 27, number 6, pages 401 –435, 1999, ISSN: 0300-5712. DOI: 10.1016/S0300-5712(99)00007-X (cited on page 3).

[16] A. Bakhshandeh, V. Qvist, and K. R. Ekstrand, "Sealing occlusal caries lesions in adults referred for restorative treatment: 2-3 years of follow-up", *Clinical Oral Investigations*, volume 16, number 2, pages 521–529, 2012, ISSN: 1432-6981. DOI: 10.1007/s00784-011-0549-4 (cited on page 3).

[17] M. Hanson and J. Pleva, "The dental amalgam issue. A review", *Experientia*, volume 47, number 1, pages 9–22, 1991, ISSN: 0014-4754. DOI: 10.1007/BF02041243 (cited on page 3).

[18] R. W. Bryant, "Dental Amalgam, by M. M. A. Vrijhoef, A. G. Vermeersch, and A. J. Spanauf", *Australian Dental Journal*, volume 27, number 1, pages 55–55, 1982, ISSN: 1834-7819. DOI: 10.1111/j.1834-7819.1982.tb04037.x (cited on page 4).

[19] A. D. Wilson and B. E. Kent, "The glass-ionomer cement, a new translucent dental filling material", *Journal of Applied Chemistry and Biotechnology*, volume 21, number 11, pages 313–313, 1971, ISSN: 1935-0554. DOI: 10.1002/jctb.5020211101 (cited on page 4).

[20] J. E. Frencken, M. C. Peters, D. J. Manton, S. C. Leal, V. V. Gordan, and E. Eden, "Minimal intervention dentistry for managing dental caries: a review", *International Dental Journal*, volume 62, number 5, pages 223–243, 2012, ISSN: 1875-595X. DOI: 10.1111/idj.12007 (cited on page 4).

[21] S. Lovesey, *Theory of Neutron Scattering from Condensed Matter*. Clarendon Press, 1984, volume 1 (cited on pages 4, 11, 19, 20, 22, 26, 73).

[22] A. Dianoux, G. Lander, P. L. G. Institut Max von Laue, and I. Laue-Langevin, *Neutron Data Booklet*. Old City, 2001. [Online]. Available: http://books.google.dk/books?id=HxAUHQAACAAJ (cited on pages 4, 19, 23).

[23] D. Brew, F. de Beer, M. Radebe, R. Nshimirimana, P. McGlinn, L. Aldridge, and T. Payne, "Water transport through cement-based barriers – A preliminary study using neutron radiography and tomography", *Nuclear Instruments and Methods in Physics Research Section A: Accelerators, Spectrometers, Detectors and Associated Equipment*, volume 605, number 1-2, pages 163 –166, 2009, ITMNR 08 - Proceedings of the sixth Topical Meeting on Neutron Radiography, ISSN: 0168-9002. DOI: 10.1016/j.nima.2009.01.146 (cited on pages 4, 5).

[24] M. Bèe, "Localized and long-range diffusion in condensed matter: state of the art of qens studies and future prospects", *Chemical Physics*, volume 292, number 2-3, pages 121 –141, 2003, Quasielastic Neutron Scattering of Structural Dynamics in Condensed Matter, ISSN: 0301-0104. DOI: 10.1016/S0301-0104(03)00257-X (cited on pages 5, 8, 32).

[25] D. A. Neumann, "Neutron scattering and hydrogenous materials", *Materials Today*, volume 9, number 1-2, pages 34 –41, 2006, ISSN: 1369-7021. DOI: 10.1016/S1369-7021(05)71336-5 (cited on page 6).

[26] J. Teixeira, M.-C. Bellissent-Funel, S. H. Chen, and A. J. Dianoux, "Experimental determination of the nature of diffusive motions of water molecules at low temperatures", *Phys. Rev. A*, volume 31, pages 1913 –1917, 3 1985. DOI: 10.1103/PhysRevA.31.1913 (cited on pages 6, 7, 16, 17, 30, 53).

[27] R Mukhopadhyay and S Mitra, "Molecular diffusion and confinement effect: Neutron scattering study", *Indian Journal of Pure and Applied Physics*, volume 44, pages 732 –740, 2006, ISSN: 0975-1041 (Online); 0019-5596 (Print). [Online]. Available: IJPAPVol.44(10)[October2006]8 (cited on page 7).

[28] R. E. Lechner, "Study of molecular rotation by quasi-elastic neutron scattering", Lecture presented at the College 4 meeting, ILL., 1971 (cited on page 8).

[29] L. Van Hove, "Correlations in space and time and born approximation scattering in systems of interacting particles", *Phys. Rev.*, volume 95, pages 249–262, 1 1954. DOI: 10.1103/PhysRev.95.249 (cited on pages 9, 22).

[30] D. J. Griffiths, *Introduction to Quantum Mechanics, 2nd edition*. Pearson Prentice Hall, 2005 (cited on pages 10, 77).

[31] G. S. Brian Martin, *Particle Physics, 3rd edition*. John Wiley & Sons, 2008, ISBN: 978-0-470-03294-7 (cited on page 10).

[32] G. Squires, *Introduction to the Theory of Thermal Neutron Scattering*. Cambridge University Press, 1978 (cited on pages 11, 13).

[33] A. Meents, S. Gutmann, A. Wagner, and C. Schulze-Briese, "Origin and temperature dependence of radiation damage in biological samples at cryogenic temperatures", *Proceedings of the National Academy of Sciences*, volume 107, number 3, pages 1094–1099, 2010. DOI: 10.1073/pnas.0905481107 (cited on page 11).

[34] R. Hempelmann, *Quasielastic Neutron Scattering and Solid State Diffusion*. Oxford University Press, 2000 (cited on pages 12, 21, 31, 73, 77).

[35] C. Kittel, *Introduction to Solid State Physics*. Wiley, 2004 (cited on page 13).

[36] J. Copley and T. Udovic, "Neutron time-of-flight spectroscopy", *Journal of Research of NIST*, 1993. [Online]. Available: http://dx.doi.org/10.6028/jres.098.006 (cited on pages 15, 16).

[37] H. N. Bordallo, L. P. Aldridge, G. J. Churchman, W. P. Gates, M. T. F. Telling, K. Kiefer, P. Fouquet, T. Seydel, and S. A. J. Kimber, "Quasi-elastic neutron scattering studies on clay interlayer-space highlighting the effect of the cation in confined water dynamics", *The Journal of Physical Chemistry C*, volume 112, number 36, pages 13 982–13 991, 2008. DOI: 10.1021/jp803274j (cited on pages 17, 18).

[38] D. Richter and T. Springer, "A twenty years forward look at neutron scattering facilities in the OECD countries and Russia", 1998. [Online]. Available: http://www.oecd.org/sti/sci-tech/1904136.pdf (cited on page 18).

[39] (Mar. 12, 2013). Ill webpage, [Online]. Available: http://www.ill.eu (cited on pages 19, 26).

[40] *Iris webpage*, Mar. 19, 2013. [Online]. Available: http://www.isis.stfc.ac.uk/instruments/iris/technical/iris-technical-information7247.html (cited on pages 19, 39).

[41] A. Foderaro, *The Elements of Neutron Interaction Theory*. Mit Press, 1971 (cited on page 21).

[42] G. H. Vineyard, "Scattering of slow neutrons by a liquid", *Phys. Rev.*, volume 110, pages 999–1010, 5 1958. DOI: 10.1103/PhysRev.110.999 (cited on pages 23, 29).

[43] J. Embs, F. Juranyi, and R. Hempelmann, "Introduction to quasielastic neutron scattering", *Zeitschrift für Physikalische Chemi*, volume 224, number 1-2, pages 5–32, 2010. DOI: doi:10.1524/zpch.2010.6090 (cited on page 24).

[44] F. G. Sànchez, "Water diffusion through compacted clays analyzed by neutron scattering and tracer experiments", PhD thesis, University of Bern, 2007 (cited on page 25).

[45] M. Bèe, *Quasielastic Neutron Scattering. Principles and Applications in Solid State Chemistry, Biology and Materials Science*. IOP Publishing Limited, 1988 (cited on pages 25–29).

[46] R. Pynn, *Neutron scattering – a primer*, 1990. [Online]. Available: http://knocknick.files.wordpress.com/2008/04/neutrons-a-primer-by-rogen-pynn.pdf (cited on page 27).

[47] V. F. Sears, "Theory of cold neutron scattering by homonuclear diatomic liquids: II. Hindered rotation", *Canadian Journal of Physics*, volume 44, pages 1299–1311, 1966 (cited on page 28).

[48] F. Volino and A. Dianoux, "Neutron incoherent scattering law for diffusion in a potential of spherical symmetry: general formalism and application to diffusion inside a sphere", *Molecular Physics*, volume 41, number 2, pages 271–279, 1980. DOI: 10.1080/00268978000102761 (cited on pages 29, 59).

[49] M.-C. Bellissent-Funel, S. H. Chen, and J.-M. Zanotti, "Single-particle dynamics of water molecules in confined space", *Phys. Rev. E*, volume 51, pages 4558–4569, 5 1995. DOI: 10.1103/PhysRevE.51.4558 (cited on pages 28, 30, 59).

[50] J. Qvist, H. Schober, and B. Halle, "Structural dynamics of supercooled water from quasielastic neutron scattering and molecular simulations.", *J Chem Phys*, volume 134, number 14, page 144 508, 2011 (cited on page 30).

[51] K. S. Singwi and A. Sjölander, "Diffusive motions in water and cold neutron scattering", *Phys. Rev.*, volume 119, pages 863–871, 3 1960. DOI: 10.1103/PhysRev.119.863 (cited on page 30).

[52] H. N. Bordallo, L. P. Aldridge, and A. Desmedt, "Water dynamics in hardened ordinary portland cement paste or concrete: From quasielastic neutron scattering", *The Journal of Physical Chemistry B*, volume 110, number 36, pages 17 966–17 976, 2006. DOI: 10.1021/jp062922f (cited on page 31).

[53] P. Heitjans and J. Kärger, *Diffusion in condensed matter: methods, materials, models*. Springer Verlag, 2005 (cited on page 31).

[54] F. Gabel, D. Bicout, U. Lehnert, M. Tehei, M. Weik, and G. Zaccai, "Protein dynamics studied by neutron scattering", *Quarterly Reviews of Biophysics*, volume 35, pages 327 –367, 04 2002. DOI: 10.1017/S0033583502003840 (cited on page 32).

[55] (May 22, 2013). Dna webpage, [Online]. Available: http://j-parc.jp/researcher/MatLife/en/instrumentation/images/DNA.jpg (cited on page 33).

[56] (May 22, 2013). In13 webpage, [Online]. Available: http://www.ill.eu/instruments-support/instruments-groups/instruments/in13/characteristics/ (cited on page 33).

[57] "ESS Technical Design Report", 2013. [Online]. Available: http://europeanspallationsource.se/documentation/tdr.pdf (cited on page 34).

[58] R. Lechner and S. Longeville, "Quasielastic neutron scattering in biology, part I: Methods", in *Neutron Scattering in Biology*, 2006, pages 309–354. DOI: 10.1007/3-540-29111-3_15 (cited on page 34).

[59] C. Carlile and M. Adams, "The design of the iris inelastic neutron spectrometer and improvements to its analysers", *Physica B: Condensed Matter*, volume 182, number 4, pages 431 –440, 1992. DOI: 10.1016/0921-4526(92)90047-V (cited on pages 35, 38).

[60] (May 22, 2013). In10 webpage, [Online]. Available: http://www.ill.eu/instruments-support/instruments-groups/instruments/in10/ (cited on page 37).

[61] *Iris user guide*, May 23, 2013. [Online]. Available: http://www.isis.stfc.ac.uk/instruments/iris/documents/iris-user-guide-201011136.pdf (cited on page 38).

[62] P. Wang, M. Ferguson, G Eng, D. Bentz, C. Ferraris, and J. Clifton, "1H nuclear magnetic resonance characterization of Portland cement: molecular diffusion of water studied by spin relaxation and relaxation time-weighted imaging", *Journal of Materials Science*, volume 33, number 12, pages 3065–3071, 1998. DOI: 10.1023/A:1004331403418 (cited on page 38).

[63] J. Greener, H. Peemoeller, C. Choi, R. Holly, E. J. Reardon, C. M. Hansson, and M. M. Pintar, "Monitoring of hydration of white cement paste with proton NMR spin–spin relaxation", *Journal of the American Ceramic Society*, volume 83, number 3, pages 623–627, 2000. DOI: 10.1111/j.1151-2916.2000.tb01242.x (cited on page 38).

[64] E. F. Rakiewicz, A. J. Benesi, M. W. Grutzeck, and S. Kwan, "Determination of the state of water in hydrated cement phases using deuterium NMR spectroscopy", *Journal of the American Chemical Society*, volume 120, number 25, pages 6415–6416, 1998. DOI: 10.1021/ja973728x (cited on page 38).

[65] E. Fratini, S.-H. Chen, P. Baglioni, and M.-C. Bellissent-Funel, "Quasielastic neutron scattering study of translational dynamics of hydration water in tricalcium silicate", *The Journal of Physical Chemistry B*, volume 106, pages 158–166, 01 2002. DOI: 10.1021/jp010536m (cited on pages 39, 40).

[66] H. Bordallo, L. Aldridge, J. Wuttke, K. Fernando, W. Bertram, and L. Pardo, "Cracks and pores – Their roles in the transmission of water confined in cementitious materials", *The European Physical Journal Special Topics*, volume 189, number 1, pages 197–203, 2010. DOI: 10.1140/epjst/e2010-01323-y (cited on pages 40, 57).

[67] H. N. Bordallo, L. P. Aldridge, and D. Arnaud, "Water dynamics in hardened ordinary portland cement paste or concrete: From quasielastic neutron scattering", *The Journal of Physical Chemistry B*, volume 110, number 36, pages 17 966–17 976, 2006. DOI: 10.1021/jp062922f (cited on pages 40, 41).

[68] I. A. E. Agency, *Neutron inelastic scattering: proceedings of symposium*, series Neutron Inelastic Scattering: Proceedings of a Symposium on Neutron Inelastic Scattering Held by the International Atomic Energy Agency in Vienna, 17-21 October, 1977. International Atomic Energy Agency, 1978 (cited on page 40).

[69] S. A. FitzGerald, D. A. Neumann, J. J. Rush, D. P. Bentz, and R. A. Livingston, "In situ quasi-elastic neutron scattering study of the hydration of tricalcium silicate", *Chemistry of Materials*, volume 10, number 1, pages 397–402, 1998. DOI: 10.1021/cm970564a (cited on page 41).

[70] (May 22, 2013). Iris data analysis web page, [Online]. Available: http://www.isis.stfc.ac.uk/instruments/iris/data-analysis/sotware-for-iris/osiris-data-analysis4697.html (cited on page 44).

[71] (May 22, 2013). Modes user guide, [Online]. Available: http://www.isis.stfc.ac.uk/instruments/iris/data-analysis/modes-v3-user-guide-6962.pdf (cited on page 44).

[72] (May 23, 2013). Dave, data analysis and visualization enviroment, [Online]. Available: http://www.ncnr.nist.gov/dave/ (cited on pages 45, 55).

[73] F. S.A., T. J.J., N. D.A., and L. R.A., "A neutron scattering study of the role of diffusion in the hydration of tricalcium silicate", *Cement and Concrete Research*, volume 32, number 3, pages 409–413, 2002. DOI: doi:10.1016/S0008-8846(01)00685-8 (cited on page 48).

[74] (Jun. 15, 2013). Lamp, large array manipulation program, [Online]. Available: http://www.ill.eu/?id=3463 (cited on page 48).

[75] V. K. Peterson and A. E. Whitten, "Hydration processes in tricalcium silicate: Application of the boundary nucleation model to quasielastic neutron scattering data", *The Journal of Physical Chemistry C*, volume 113, number 6, pages 2347–2351, 2009. DOI: 10.1021/jp807209w (cited on page 49).

[76] H. N. Bordallo, L. P. Aldridge, P. Fouquet, L. C. Pardo, T. Unruh, J. Wuttke, and F. Yokaichiya, "Hindered water motions in hardened cement pastes investigated over broad time and length scales", *ACS Applied Materials & Interfaces*, volume 1, number 10, pages 2154–2162, 2009. DOI: 10.1021/am900332n (cited on pages 52, 60).

[77] T. Takamuku, M. Yamagami, H. Wakita, Y. Masuda, and T. Yamaguchi, "Thermal property, structure, and dynamics of supercooled water in porous silica by calorimetry, neutron scattering, and NMR relaxation", *The Journal of Physical Chemistry B*, volume 101, number 29, pages 5730–5739, 1997. DOI: 10.1021/jp9631238 (cited on page 53).

[78] W. P. Gates, H. N. Bordallo, L. P. Aldridge, T. Seydel, H. Jacobsen, V. Marry, and G. J. Churchman, "Neutron time-of-flight quantification of water desorption isotherms of montmorillonite", *The Journal of Physical Chemistry C*, volume 116, number 9, pages 5558–5570, 2012. DOI: 10.1021/jp2072815 (cited on page 53).

[79] R. Berliner, M. Popovici, K. Herwig, M. Berliner, H. Jennings, and J. Thomas, "Quasielastic neutron scattering study of the effect of water-to-cement ratio on the hydration kinetics of tricalcium silicate", *Cement and Concrete Research*, volume 28, number 2, pages 231 –243, 1998. DOI: http://dx.doi.org/10.1016/S0008-8846(97)00260-3 (cited on page 63).

[80] E. Fratini, F. Ridi, S.-H. Chen, and P. Baglioni, "Hydration water and microstructure in calcium silicate and aluminate hydrates", *Journal of Physics: Condensed Matter*, volume 18, number 36, S2467, 2006. DOI: doi:10.1088/0953-8984/18/36/S18 (cited on page 63).

[81] M. Avrami, "Kinetics of phase change. i general theory", *The Journal of Chemical Physics*, volume 7, number 12, pages 1103–1112, 1939. DOI: 10.1063/1.1750380 (cited on page 63).

[82] M. Avrami, "Kinetics of phase change. ii transformation-time relations for random distribution of nuclei", *The Journal of Chemical Physics*, volume 8, number 2, pages 212–224, 1940. DOI: 10.1063/1.1750631 (cited on page 63).

[83] M. Avrami, "Granulation, phase change, and microstructure kinetics of phase change. iii", *The Journal of Chemical Physics*, volume 9, number 2, pages 177–184, 1941. DOI: 10.1063/1.1750872 (cited on page 63).

[84] C. Davidson and I. Mjör, *Advances in glass-ionomer cements*. Quintessence Pub. Co., 1999 (cited on pages 63, 66–68).

[85] T. I. Barry, D. J. Clinton, and A. D. Wilson, "The structure of a glass-ionomer cement and its relationship to the setting process", *Journal of Dental Research*, volume 58, number 3, pages 1072–1079, 1979. DOI: 10.1177/00220345790580030801 (cited on pages 67, 68).

[86] S. Crisp and A. D. Wilson, "Reactions in glass ionomer cements: III. The precipitation reaction", *Journal of Dental Research*, volume 53, number 6, pages 1420–1424, 1974. DOI: 10.1177/00220345740530062101 (cited on page 68).